

A conserved logic for the development of cortical layering in tetrapods

Authors: Astrid Deryckere^{1†}, Saket Choudhary^{2,3‡}, Connor Lynch^{4,5}, Lian Kirit V. P. Limperis¹,
Pauline Affatato¹, Jamie Woych¹, Elias Gumnit¹, Alonso Ortega Gurrola¹,
Rahul Satija^{2,3}, Christian Mayer⁴, Maria Antonietta Tosches^{1*}

Affiliations:

¹ Department of Biological Sciences, Columbia University; New York, 10027 NY, USA.

² New York Genome Center; New York, 10013 NY, USA

³ Center for Genomics and Systems Biology; New York University, New York, 10003 NY, USA.

⁴ Max Planck Institute for Biological Intelligence; Martinsried, D-82152, Germany.

⁵ Graduate School of Systemic Neurosciences; Ludwig Maximilian University (GSN-LMU),
Munich, D-82152, Germany.

*Corresponding author. Email: mt3353@columbia.edu

Present addresses:

[†] Laboratory of Reproductive Genomics, KU Leuven; Leuven, 3000, Belgium

[‡] Koita Centre for Digital Health, IIT Bombay; Mumbai, 400076, India

Abstract: The evolutionary origin of the cerebral cortex, a brain region typically defined by the presence of neuronal layers, remains elusive. While mammals and reptiles have a layered cortex, the amphibian pallium (dorsal telencephalon) is considered unlayered. Here, we identify distinct superficial- and deep-layer neurons in the salamander pallium. Like in mammals, these layers develop sequentially from multipotent radial glia and intermediate progenitor cells. Using lineage tracing and scRNA-seq, we reveal conserved principles of cortical development, including the temporal patterning of radial glia and the association of neuronal birthdate, molecular identity, and projection type. Our findings indicate that the mammalian cortex evolved from this ancestral developmental template through the inversion of the corticogenesis gradient, from outside-in to inside-out, and the diversification of neuronal differentiation programs.

Main Text:

Introduction

30 By building associations between sensory inputs, internal states, and prior experiences, the cerebral cortex enables flexible behavior and advanced cognition. However, how the cortex arose in vertebrates and how it gained a complex organization in mammals remain long-standing questions in neuroscience. The cerebral cortex is part of the pallium, the dorsal subdivision of the telencephalon present in all vertebrates (1). While some regions of the pallium
35 have neurons arranged into nuclei, the cerebral cortex is anatomically defined as “a *neural aggregate that consists of alternating layers of different neuronal populations and their associated fibers*” (2). The “*different neuronal populations*” are glutamatergic neurons (mostly pyramidal types), while GABAergic interneurons are instead scattered across all layers. According to this definition, the only vertebrates with a true cerebral cortex are mammals and
40 non-avian reptiles. Indeed, the cerebral cortex has long been considered an amniote innovation (a layer-like organization may have evolved independently in birds (3–5)).

With its six layers, the mammalian neocortex has been extensively studied at the developmental, anatomical, and functional levels. But besides a six-layered neocortex, mammals also have cortical regions with fewer layers (6). The simplest mammalian cortices are
45 the hippocampus and the piriform cortex, which resemble at the gross anatomical level the cerebral cortex of non-avian reptiles. In these cortices, traditionally described as three-layered, a layer of neuronal cell bodies is found between two layers made mostly of fibers (axons and dendrites) (7). Detailed anatomical and molecular studies, however, have shown that these simple reptilian and mammalian cortices also comprise sublayers of glutamatergic neurons, with
50 distinct gene expression profiles and input-output connectivity (5, 8–14). Therefore, amniote cortices, from simple to complex, are made of different glutamatergic neuron types organized into layers.

Cortical layers are not just an anatomical feature; they are part of the implementation of a successful biological architecture for associative learning (15–18). In all cortices, fibers are
55 arranged in an orthogonal grid, where the pyramidal neurons' dendrites extend along the radial axis (from ventricle to surface) and incoming axons along the tangential axis (parallel to the cortical surface). Inputs from distinct brain regions target specific cortical depths, where they synapse on the dendrites of broadly distributed neuronal populations. As a result, neurons in different layers integrate distinct sets of inputs, and each neuronal layer functions as a parallel
60 processing unit (19). This architecture makes the cerebral cortex an efficient, flexible, and expandable layout for associative learning and memory storage (20–23). Understanding the origin and evolution of cortical layering is thus essential to elucidate the emergence of cortical computations.

65 Classical neuroanatomical studies did not identify layers of distinct neuron types in the pallia of
fish and amphibians (anamniotes), leading to the idea that a true cerebral cortex is an amniote
innovation. In teleosts, the pallium is an aggregate of nuclei, while in lampreys, certain sharks,
lungfishes, and amphibians, it comprises densely-packed cell bodies near the ventricle and a
fiber-rich zone closer to the pial surface (24–26). Notably, in amphibians, axons and dendrites
70 are arranged orthogonally, and projections from intra- and extra-pallial areas terminate at
different depths in the fiber layer, suggesting a form of laminar input sorting similar to that in
amniotes (27, 28). Furthermore, our previous work suggests the existence of at least two
molecularly-distinct neuronal populations organized in separate layers in the salamander dorsal
pallium (29). These observations raise the question of whether a layered cerebral cortex
predates amniotes.

75 In the mammalian cerebral cortex, layers are made of distinct neuron types that are generated
by multipotent radial glia progenitors in a stereotyped developmental sequence (30–32). This
mechanism is distinct from layer formation in other parts of the brain, like the cerebellum and the
superior colliculus (33, 34). What is truly peculiar about the cerebral cortex is that neuronal
birthdate is coupled with molecular identity, projection identity, and layer allocation (10, 11, 35–
80 37). Importantly, this temporal control of corticogenesis has functional relevance, because it may
fine-tune circuit assembly (38–41). Therefore, we asked whether the same principles for layer
formation apply to the amphibian pallium, to test the hypothesis that corticogenesis relies on
developmental programs conserved across tetrapods.

In this study, we demonstrate that "*layers of different neuronal populations*" (2) are present in
85 the amphibian dorsal pallium. By uncovering the cellular and molecular bases of pallial
neurogenesis in the salamander *Pleurodeles waltl*, we identify striking parallels with mammalian
corticogenesis. First, in the salamander dorsal pallium, neuronal birthdate is linked to molecular
identity, layer position, and projection type, similar to mammals. Second, layers are generated
by multipotent radial glia progenitors that express a common set of temporally-modulated genes
90 in both salamander and mouse. Third, we show that intermediate progenitor cells - a committed
progenitor type that amplifies the neuronal output - also exist in salamanders and are not an
amniote innovation. Our analysis also reveals striking differences across species: in amphibians
and mammals, neuronal differentiation programs diverge after cell cycle exit. Furthermore, early-
born and late-born neurons have opposite distributions along the radial axis, following an
95 ancestral outside-in pattern in amphibians in contrast to the inside-out pattern in mammals. Our
results challenge the view that a layered cerebral cortex is an amniote innovation, and reveal
critical novelties in cortical neurogenesis that produced more complex cerebral cortices in
mammalian ancestors.

100 Results

The adult salamander dorsal pallium includes two layers of glutamatergic neurons

The dorsal pallium of amphibians, including the salamander, was previously described as non-laminated (25). Recently, we built a comprehensive single-cell RNA sequencing (scRNA-seq) dataset of the adult salamander forebrain and identified six distinct clusters of glutamatergic
105 neuron types mapping to the dorsal pallium (DP), the pallial region nested between the medial pallium (hippocampal homolog) and the olfactory pallium (lateral and ventral pallium) (29, 42). Here, we further analyzed the spatial distribution and differential gene expression of DP clusters (telencephalic glutamatergic (TEGLU) neuron clusters 8-11, 13 and 20) (Fig. 1A,B). DP neurons could be classified in superficial layer (DP-SL) and deep layer (DP-DL) types, based on the
110 differential expression of hundreds of genes, including transcription factors, neuropeptides, and proteins involved in axonal pathfinding and synaptogenesis (Fig. 1B–F, fig. S1A–C). Superficial-layer neurons (cluster TEGLU20) uniquely expressed the neuropeptide precursor gene *Nts* and the transcription factor *Foxp1* at high levels, and were transcriptomically distinct from other *Nts*-
115 GABAergic interneurons in deep layers (Fig. 1E"). Conversely, deep-layer neurons (clusters TEGLU 8-11, 13) uniquely expressed protein phosphatase and calcium sensing proteins *Ppm1h* and *Otof* (fig. S1C). These neurons showed further heterogeneity based on their anterior-posterior and mediolateral position. For our developmental analysis, we focused on the anterior DP, where *Nts*-expressing neurons are more abundant. The anterior DP was identified by the
120 expression of *Frmd8* in the deep layer; these neurons also expressed the transcription factor *Nfia* (clusters TEGLU8, 10, 11, Fig. 1D–F, fig. S1G). The posterior DP, demarcated by *Nr2f2* expression (cluster TEGLU9), and a population of *Calb2* expressing neurons (cluster TEGLU13) at the boundary between DP and lateral pallium (LP) (fig. S1C and (29)), were excluded from subsequent analysis.

125 ***Pallial layers are generated sequentially during development***

We next asked whether the two layers in the anterior DP are generated sequentially over time during development, as are layers in the mammalian cerebral cortex. In *Pleurodeles* larvae, pallial neurogenesis spans approximately three months (43, 44), and previous work, including
130 intraventricular AAV injections at different developmental timepoints (45), suggested that neurons in different positions along the radial axis are generated at different time points during development. We thus designed a birthdating experiment where we administered the thymidine analog EdU to separate cohorts of larvae at different developmental stages, and then assessed EdU labeling in post-metamorphic juveniles, when neurons have integrated into mature circuits
135 (44) (Fig. 1G). Since EdU gets diluted with every cell cycle, only cells that exit the cell cycle around the time of EdU injection will retain EdU labeling at the experimental endpoint. In the pallium, early EdU administration resulted in labeling of superficial neurons, while later EdU injections produced labeling in neurons progressively closer to the ventricle, indicating that

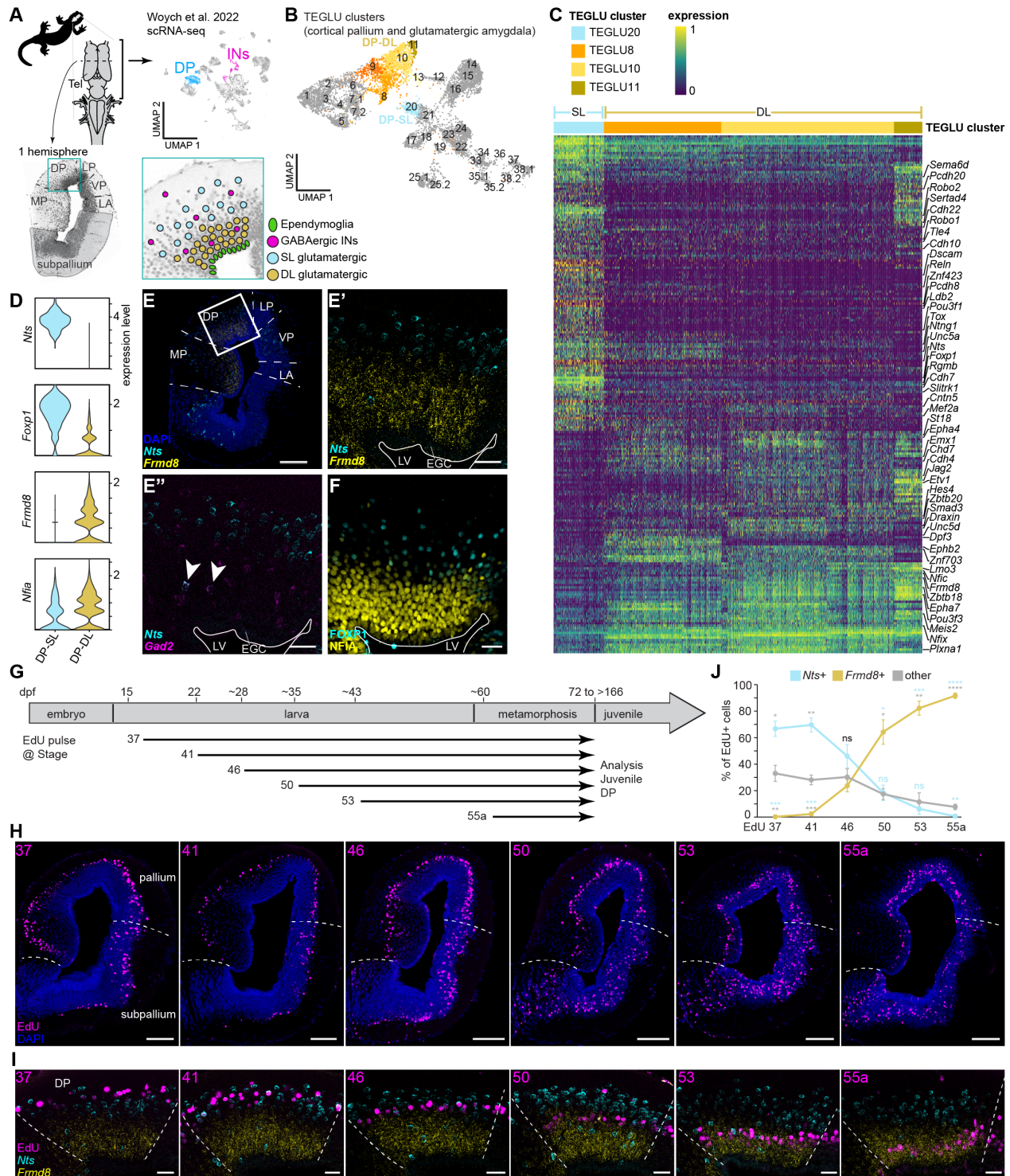


Fig. 1. Two distinct layers of glutamatergic neurons are generated sequentially in the salamander dorsal pallium. (A) Position and cellular heterogeneity of the salamander DP. (B) UMAP plot of clusters of glutamatergic neurons from the salamander cortical pallium and glutamatergic amygdala, with highlighted dorsal pallium clusters, data from (29). (C) Heatmap showing differentially expressed genes in superficial- and deep-layer DP neurons, with transcription factors, neuropeptides and genes involved in axon guidance and cell migration/communication highlighted. (D) Violin plots showing the expression of *Nts*, *Foxp1*, *Frmd8* and *Nfia* in the superficial- and deep-layer DP neurons. (E) Expression of the superficial-layer marker *Nts* and the deep-layer marker *Frmd8* in the salamander telencephalon (E) and dorsal pallium (E'); expression of *Nts* and *Gad2* in dorsal pallium, showing co-expression only

in scattered deep layer interneurons (arrowheads) (E"). All markers detected by HCR. (F) Expression of transcription factors FOXP1 and NFIA in the salamander dorsal pallium, detected by immunohistochemistry. Scale bar 200 μ m in overview image (E) and 50 μ m in magnifications (E', E", F). (G) Birthdating study design, showing salamander development, and time points of EdU injection. (H) Coronal sections at mid-telencephalic level in the juvenile salamander showing the presence of EdU-labeled cells according to the time of injection. White dashed lines depict the pallial-subpallial borders, scale bars 200 μ m. (I) Magnification of the dorsal pallium, showing co-labeling of EdU with *Nts* or *Frdm8* (HCRs). White dashed lines depict the borders of the DP, scale bars 50 μ m. (J) Relative number of EdU+ cells co-expressing *Nts* or *Frdm8* for each injection time. $n = 4$ for each injection time, except 55a where $n = 5$, error bars represent standard deviation. Statistical significance was assessed by repeated-measures two-way ANOVA with Geisser-Greenhouse correction, followed by Tukey's multiple comparisons test (* $p < 0.05$, ** $p \leq 0.01$, *** $p \leq 0.001$, **** $p \leq 0.0001$) and is indicated above the data point, with the color of the asterisk corresponding to the comparison.

Abbreviations: DL, deep-layer neurons; DP, dorsal pallium; dpf, days post fertilization; EGC, ependymoglia cells; INs, interneurons; LA, lateral amygdala; LP, lateral pallium; LV, lateral ventricle; MP, medial pallium; SL, superficial-layer neurons; TEGLU, telencephalic glutamatergic; Tel, telencephalon; VP, ventral pallium

140 salamander pallial neurogenesis follows an outside-in pattern, where early-born neurons are superficial and late-born neurons are deeper. In contrast, neurons in the subpallium, especially the striatum, integrated over the full thickness of the mantle zone, regardless of their birthdate (Fig. 1H). Overlaying the expression of the superficial-layer neuron marker *Nts* and deep-layer marker *Frdm8* with the EdU signal revealed that early-born and late-born neurons in the DP are not only distinct in their laminar positioning, but also in their molecular identity (Fig. 1I).
145 Quantification suggests that at the population level, neural progenitors in the DP gradually switch from making *Nts*+ superficial-layer to *Frdm8*+ deep-layer neurons around stage 50 (mid-neurogenesis) (Fig. 1J). These results reveal a conserved principle of cortical development in amphibians and mammals: the sequential, time-dependent generation of neurons with distinct molecular identities and specific positions along the radial axis.

150 ***Pallial radial glia are multipotent***

Two alternative scenarios could explain the sequential generation of salamander superficial- and deep-layer neurons from radial glia progenitors (Fig. 2A). One scenario is that DP radial glia are unipotent, with distinct "early" and "late" radial glia types and lineages. "Early" radial glia would be active in early neurogenesis, and cease to proliferate or exist around stage 50, whereas
155 "late" radial glia would be quiescent in early neurogenesis, and activated only around stage 50. Alternatively, DP radial glia may be multipotent, like most radial glia in the mammalian neocortex (part of the mammalian dorsal pallium) (31), with the same progenitor cell switching from producing superficial- to deep-layer neurons around stage 50.

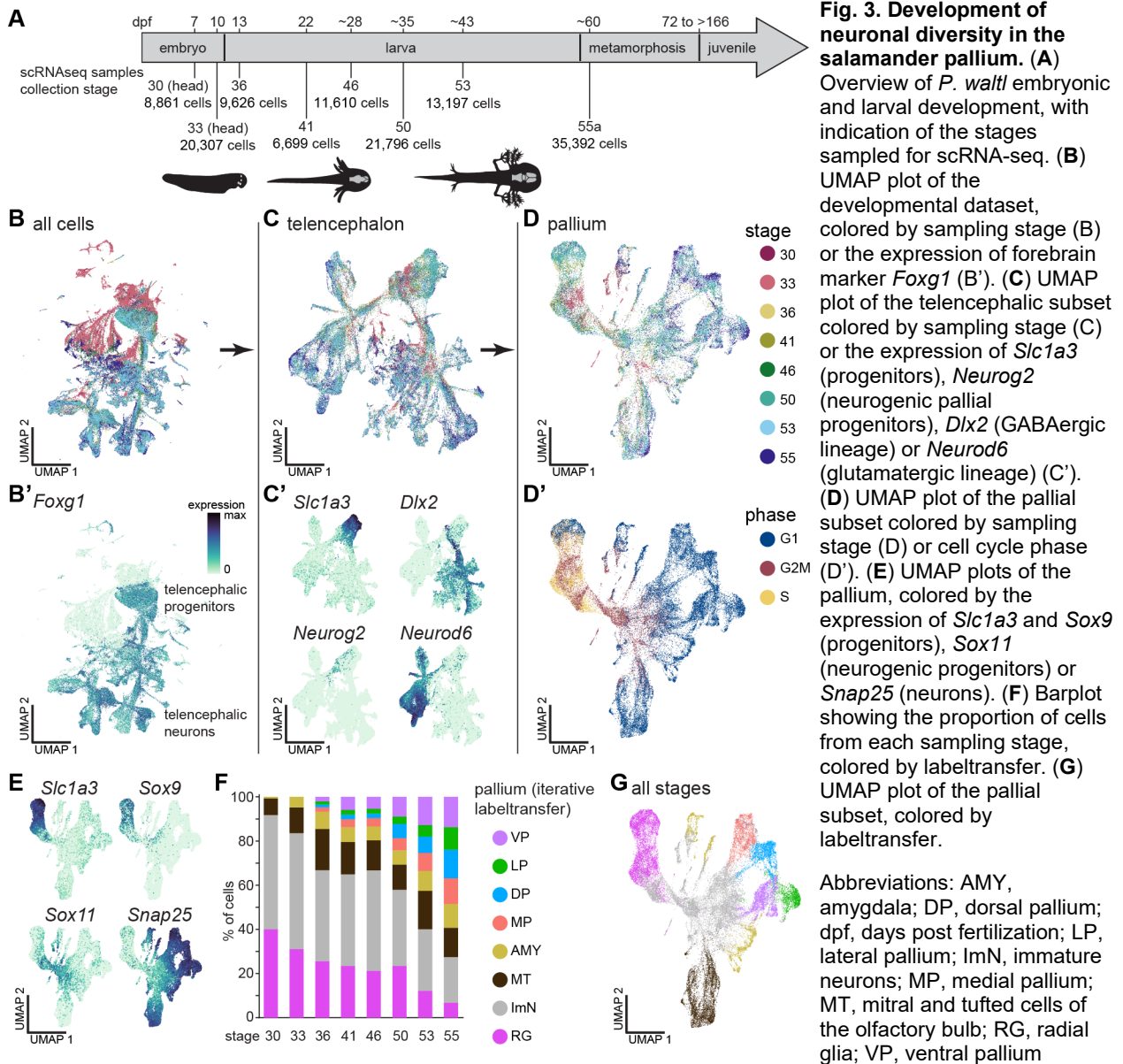
To test these two hypotheses, we used a barcode-based lineage tracing technique called
160 TrackerSeq, where a barcoded eGFP library is stably integrated in neural progenitors with a PiggyBac transposase, and then barcodes and cellular transcriptomes are retrieved with scRNA-seq to reconstruct lineage relationships (46). We electroporated the developing salamander pallium with a TrackerSeq library at stage 39, one of the earliest stages amenable to electroporation of the telencephalon, when the production of superficial neurons peaks (Fig. 1J, 2B). Animals were allowed to complete larval development and metamorphosis (3.5 - 6.5 months), after which we confirmed the stable expression of eGFP, and observed groups of

spatially-contiguous eGFP+ cells spanning the entire thickness of the pallium (**Fig. 2B**). We then dissociated the electroporated forebrains, FACS-sorted eGFP+ cells, and prepared single-cell
170 sequencing libraries for both the transcriptomes and lineage barcodes (**Fig. 2B**). Eight libraries, each containing traced cells from two animals, were sampled, resulting in the recovery of 8,011 cells. To assign clonal relationships, we identified connected components in a graph constructed from TrackerSeq barcode signatures (see **Methods**). This led to the recovery of 1,158 cells, each sharing a lineage barcode with at least one other cell in the dataset, resulting in 285
175 "multicell" clones (**Tables S1, S2 and figs. S2-S6**). To examine the cellular composition of the lineages, we annotated the entire dataset using established cell type marker genes (29) (**Fig. 2C-E**). We counted the number of cells with clonal intersections between annotated groups. Twenty-two clones in the dataset included superficial- and deep-layer neurons (**Fig. 2F,G**). Other clones included postmitotic DP neurons and immature neurons and/or ependymoglia cells
180 (salamander neural stem cells directly derived from radial glia progenitors) (**Fig. 2F-H**). Using these counts, we calculated a z-score for each pairwise set of groups (47). This coupling analysis demonstrated a significant clonal relationship between superficial- and deep-layer DP neurons (**Fig. 2H**). Hierarchical clustering of the pairwise correlations between the coupling scores revealed strong correlations between the superficial- and deep-layer DP neurons (**fig. S6A**), further indicating that these cell types originated from the same progenitor during
185 development. These data reveal a second conserved principle of corticogenesis: the generation of superficial and deep layer neurons by multipotent radial glia progenitors.

Pallial radial glia progenitors are heterogeneous in space and time

Next, we sought to elucidate how superficial- and deep-layer neurons are specified from radial
190 glia progenitors at the molecular level. For this, we built a scRNA-seq atlas of the developing salamander brain (**Fig. 3A, fig. S7**) including eight stages sampled over 2 months of development, from stage 30 (7-day-old embryo) to stage 55a (last stage before metamorphosis), significantly expanding on our previously published dataset (29). Our final dataset included 127,488 high-quality cells, grouped in 14 major neuronal and non-neuronal clusters (**Fig. 3B, fig. S7A,B**), which we annotated based on the expression of well-established marker genes (**fig. S7B-D**). Next, we filtered the dataset for telencephalic progenitor cells and neurons, defined as *Foxg1*-expressing cells (**Fig. 3B',C**), and subsequently retained only cells of the pallium, expressing glutamatergic markers (*Neurog* and *NeuroD* genes) and not GABAergic markers (e.g. *Dlx* genes) (**Fig. 3C'-D'**, see **Methods**). Cells in the UMAP projection were arranged
200 according to the expression of general markers of neuronal differentiation; from cells expressing the radial glia markers *Slc1a3* and *Sox9*, to cells expressing the neural progenitor marker *Sox11*, and then cells expressing mature neuron markers such as the synaptic gene *Snap25* (**Fig. 3G**). To annotate this dataset, we used an iterative supervised learning approach to transfer cell type annotations from our adult cell type atlas (29) to the developmental dataset
205 (**fig. S7E**, see **Methods**). The stage 30 dataset was dominated by progenitor cells and immature neurons, and the relative proportion of differentiated neurons increased in subsequent stages.

Similar to the mammalian pallium (48, 49), we observed the first differentiated neurons in the olfactory bulb (OB), followed by ventral regions (amygdala, and ventral pallium) and then more dorsal regions (lateral, dorsal and medial pallium) (Fig. 3F,G), consistent with (44).



210 Similar to the mammalian cortex, proliferative radial glia in the salamander pallium express *Gfap*, *Sox2*, and *Sox9* (29, 44), have a soma in the ventricular zone, and a thin fiber extending multiple endfeet to the pial surface (Fig. 4A,B, fig. S7C). Studies on the mouse neocortex have identified the temporal molecular states of radial glia progenitors that underlie the generation of early- and late-born neurons (50). We thus asked whether salamander radial glia exist in distinct

215 temporal states as well. In our dataset, however, radial glia cells were sampled from different developmental stages, as well as from different spatial domains (pallium and subpallium, and their subdivisions). We reasoned that the transcriptomic diversity of radial glia was the

combination of spatial and temporal gene expression signatures, plus other known sources of technical and biological heterogeneity (e.g. number of genes and of UMIs per cell, cell cycle phase). Therefore, we first disentangled the spatial heterogeneity of radial glia cells, to then focus on dorsal pallium radial glia and analyze their temporal heterogeneity (**Fig. 4C**). We selected cycling progenitor cells with high expression levels of *Slc1a3*, *Gfap*, *Sox2* and *Fabp7* (also known as BLBP), and absence of *Neurog2* (i.e. not yet committed to a neuronal fate) from the pallial dataset (**fig. S8A**). After clustering, we identified and filtered out radial glia cells that exited the cell cycle and acquired an astroglial fate (reduced expression of *Pcna* and *Mcm2* and high levels of astrocyte markers such as *Aqp4*, *Slc13a5*, *Acan*) (44) (**Fig. 4C, fig. S8B,C**). We then performed a principal component analysis (PCA), after regressing out the effect of known sources of technical and biological variation including the sampling stage (**fig. S8D**), and finally projected the cells on the principal curve that captures the remaining sources of transcriptomic heterogeneity (**Fig. 4C**). A total of 1,783 genes (947 increasing and 836 decreasing) had significant expression variation along this principal curve, with the majority of differentially expressed genes following an expression gradient rather than displaying sharp boundaries. We hypothesized that this principal curve correlated with the medio-lateral position of pallial radial glia, as suggested by the expression of several genes at the two extremes of this axis, including *Wnt8b* and the Wnt antagonist *Sfrp1* (**Fig. 4D**). In salamanders (51, 52) and other vertebrates, Wnt and anti-Wnt signaling molecules define the hem and the anti-hem, two major telencephalic signaling centers at opposite ends of the pallial mediolateral axis. We then clustered pallial radial glia based on these varying genes (**fig. S8E**) to identify major spatial domains. Validation in the stage 50 telencephalon confirmed that these clusters correlated with regional boundaries along the mediolateral axis. *Slit2* and *Dmrt3* were restricted to medial pallium (MP) radial glia, while *Wnt8b* expression extended to part of the DP, although at lower levels. Furthermore, *Meis2* expression was upregulated in DP and peaked in LP, whereas *Sp8* and *Sfrp1* expression spanned the most ventral parts of the pallium (**Fig. 4E, fig. S8F-L**). With these analyses, we were able to identify DP radial glia cells (**Fig. 4C,F**).

Next, we analyzed the remaining sources of transcriptomic heterogeneity in DP radial glia. We again performed PCA, after regressing out known sources of variation including the medio-lateral gradient, but excluding sampling stage, and fit a principal curve. The position of cells along this curve correlated with developmental stage, suggesting that this curve captured the maturation of the DP progenitors over time (**fig. S9A**). Hundreds of genes displayed either decreasing or increasing expression along this axis of variation (**fig. S9B, Table S3**). We then performed the same analysis on a mouse neocortical dataset (53) to identify temporal genes in mouse radial glia cells between stages E11.5 and E15.5. Finally, we compared radial glia temporal genes in salamander and mouse. Among salamander-mouse one-to-one orthologs, 316 (188 upregulated and 128 downregulated) genes in salamanders and 380 (168 upregulated and 212 downregulated) genes in mouse showed differential expression across the maturation axis. Of those, a significant subset (218 genes) showed conserved differential expression in mouse and salamanders (**Fig. 4F,G, Table S4**). The genes upregulated over developmental

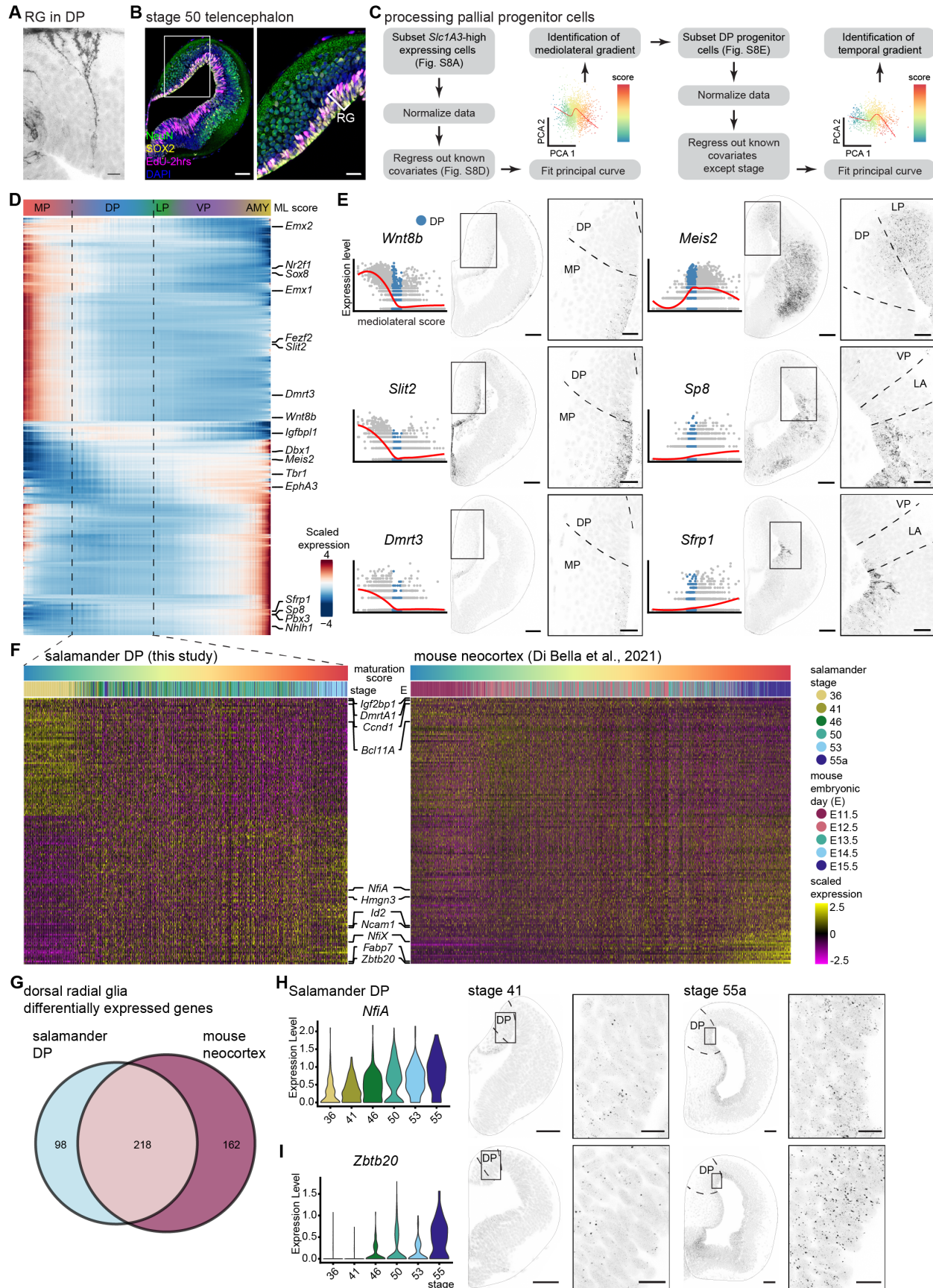


Fig. 4. Spatial and temporal patterning of pallial radial glia. (A) Visualization of a radial glia cell in the salamander DP through electroporation of membrane-bound GFP at stage 53. (B) Coronal section through the telencephalon of a stage 50 larva, injected with EdU 2 hrs before euthanasia, showing immunoreactivity for NEUN (neurons), SOX2 (radial glia) and EdU (proliferative cells). (C) Schematic representation of the analysis. (D) Heatmap showing differentially expressed genes in pallial radial glia cells, ordered along the principal curve representing the mediolateral score. (E) Left: expression (normalised molecules per cell) of canonical markers of mediolateral specification as a function of mediolateral score. The red curve shows local averaging (loess smoothing). Dorsal pallium cells highlighted in blue. Right: gene expression in the telencephalon (HCRs) and magnification. Scale bars in overview 100 μ m, in magnifications 40 μ m. (F) Heatmaps showing differentially expressed genes in salamander DP radial glia (left) and mouse neocortical radial glia (right, data from (53)) arranged along the principal curve representing the maturation score. (G) Venn diagram representing differentially expressed genes along the maturation principal curve in salamander and mouse dorsal radial glia (overlapping p-value < 1e-16 after Fisher's exact test). (H,I) Validation of the maturation score, showing expression of *Nfia* and *Zbtb20* in the scRNA-seq dataset (H, violin plots) and in the salamander telencephalon at early (left) and late (right) developmental stages (I). Scale bars in overview 100 μ m, in magnifications 20 μ m.

Abbreviations: DP, dorsal pallium; EP, electroporation; HCR, hybridization chain reaction in situ hybridization; LA, lateral amygdala; LP, lateral pallium; ML, mediolateral; MP, medial pallium; RG, radial glia; VP, ventral pallium

260 time in both species showed enrichment for gene ontology categories such as gliogenesis and
glial cell differentiation, while genes downregulated over time in both species were associated
with RNA/DNA regulatory functions (**fig. S9C**). Among these shared temporal genes, we found
the transcription factors *Nfia*, *Nfix*, and *Zbtb20*, well-known temporal transcription factors in
mammalian neural development (54–59). Validating these results, HCRs showed higher
265 expression of *Nfia* and *Zbtb20* in dorsal pallium radial glia in late (stage 55a) compared to early
(stage 41) salamander larvae (**Fig. 4H,I**). Altogether, these results indicate that in salamander
and mouse, dorsal radial glia exist in two conserved temporal states, defined by the expression
of a conserved set of temporal genes.

Intermediate progenitor cells in the developing salamander pallium

270 The molecular similarity of radial glia progenitors in amphibians and mammals contrasts with the
wide transcriptomic divergence of differentiated pallial neurons across species (29). To
understand how different neuron types can emerge from a conserved developmental blueprint,
we sought to compare differentiation trajectories inferred from salamander and mouse datasets.
After excluding cells of extra-pallial origin, we applied URD trajectory inference to our entire
salamander scRNA-seq pallial dataset (see **Methods**). This approach orders cells according to
275 pseudotime (**fig. S10A**), and then generates a trajectory tree based on transcriptomic similarity
(60). The resulting tree shows divergence of differentiation trajectories after cell cycle exit,
starting from stage 33, and is consistent with current knowledge on pallial regions. Specifically,
the first split in the URD tree separates the precursors of OB mitral/tufted cells from the rest of
pallial cells, and is followed by a split between dorsomedial and ventrolateral pallial cells, in line
280 with our previous results (29) and the expression of key regional marker genes (**Fig. 5A-C, fig.
S10B**). From an analysis of genes dynamically expressed along the pseudotime axis, we
observed that cells first expressed radial glia markers like *Slc1a3*, *Pax6*, *Sox2* and *Sox9*,
followed by the Notch receptor *Dll1* and the transcription factors *Nhlh1*, *Insm1*, *Sox4*, and
Eomesodermin (*Eomes*), which encodes for T-box protein 2 (*Tbr2*), and finally *Syt1*, *Snap25*
285 and *Slc17a7*, markers of differentiated neurons (**Fig. 5D,E, fig. S10C**). Interestingly, *Dll1*, *Nhlh1*,

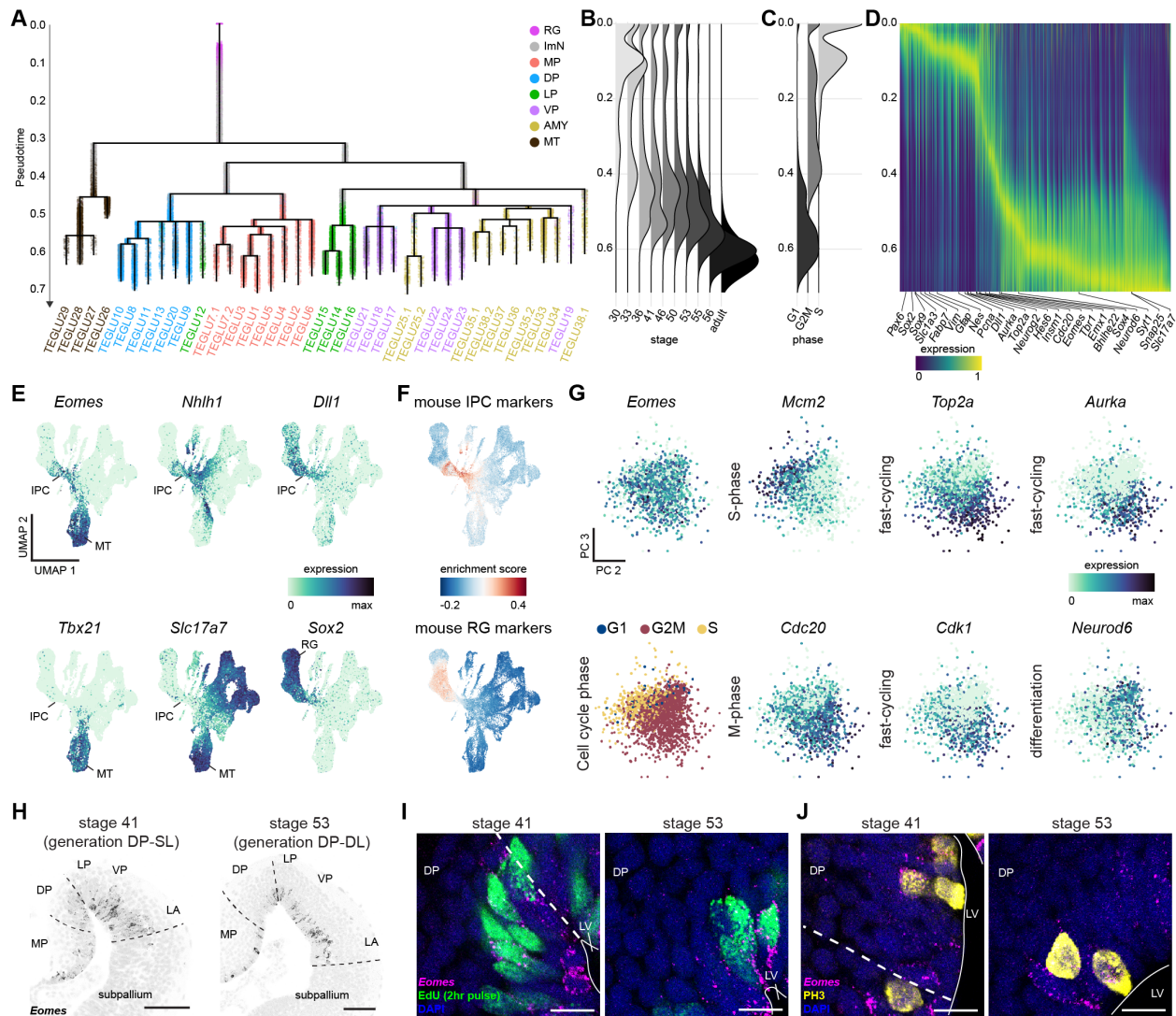


Fig. 5. Proliferative *Eomes*⁺ intermediate progenitor cells in the salamander pallium. (A) URB branching tree with 4751 cells ordered by pseudotime, with cells expressing high levels of *Slc1a3* as root, and adult differentiated neurons as tips. Cells are color-coded by their regional identity. (B,C) Distribution of cells according to sampling stage (B) or cell cycle phase (C) along the URB pseudotime axis. (D) Smoothed heatmap of genes with variable expression in pallium cell trajectories along pseudotime. Only genes expressed in both SL and DL trajectories are shown. (E) UMAP plots of the pallium dataset colored by the expression of *Eomes*, *Nhlh1*, *Dll1* (intermediate progenitor cells), *Tbx21* (mitral and tufted cells of the olfactory bulb), *Slc17a7* (glutamatergic neurons), and *Sox2* (RG progenitors). (F) UMAP plots of the salamander pallium dataset colored by the enrichment score (Seurat module score) for mouse IPC (top) and RG (bottom) marker genes. (G) *Eomes*⁺ *Slc17a7*-negative cells (IPCs) in principal components (PC) space, showing subpopulations according to the expression of proliferation and differentiation markers, as well as cell cycle phase. (H) Coronal sections through the stage 41 (left) and stage 53 (right) dorsal telencephalon, showing the expression of *Eomes* in scattered cells in the pallial ventricular zone. (I,J) Magnifications of the dorsal pallium ventricular zone, showing co-expression of *Eomes* with EdU (2hr pulse, S-phase) (I) or PH3 (M-phase) (J). Scale bars in H 100 μ m, in I-J 20 μ m.

Abbreviations: DL, deep layer neurons; DP, dorsal pallium; ImN, immature neurons; IPC, intermediate progenitor cell; LA, lateral amygdala; LP, lateral pallium; LV, lateral ventricle; MP, medial pallium; MT, mitral/tufted cells; PH3, phospho-histone H3; RG, radial glia; SL, superficial layer neurons; St, stage; VP, ventral pallium.

Insm1, and *Eomes* are key markers for intermediate progenitor cells (IPCs) in the embryonic subventricular zone (SVZ) of the mammalian neocortex (61, 62). These transient-amplifying

progenitor cells are classically considered an amniote innovation and believed to contribute to the expansion of the neocortex (63–65). However, extending the comparative analysis to the entire transcriptome, we found that the expression of mouse IPC- and radial glia-specific genes was enriched in salamander *Eomes+*/*Slc17a7-* and *Pax6+*/*Sox2+* cells, respectively (**Fig. 5E,F**). A closer inspection of *Eomes+*/*Slc17a7-* cells in the transcriptomics space revealed that these cells exist in distinct proliferative states (**Fig. 5G**). As described for mouse *Eomes+* cells (66), one subpopulation expressed genes associated with highly proliferative cells (*Top2A*, *Cdk1*, *AurkA*), while a second group appears to be exiting the cell cycle, upregulating differentiation genes such as *NeuroD6* (**Fig. 5G**). HCR revealed *Eomes* mRNA in a subset of cells in the ventricular zone of the salamander pallium, both in early and late developmental stages (**Fig. 5H**). To validate whether these *Eomes* cells are proliferative like mammalian IPCs and as indicated by the scRNAseq data (**Fig. 5C,D**), we detected S-phase cells after EdU administration and stained M-phase cells with a phospho-histone H3 antibody. Both methods revealed the presence of proliferative *Eomes+* cells in the salamander ventricular zone (**Fig. 5I,J**). Together, these results indicate that *Eomes+* IPCs are not a mammalian innovation, but a conserved progenitor type in vertebrate pallial development.

Conserved projection classes from diverging neuronal differentiation programs

Our comparison of salamander and mouse progenitors revealed striking transcriptomic similarities in radial glia and intermediate progenitors, as well as the conservation of radial glia temporal states. We thus wondered how these progenitors generate diverging sets of glutamatergic neurons in salamanders and mammals. Trajectory analyses show that neurons become increasingly distinct at the transcriptomic level as they differentiate (**Fig. 5A**, (53, 67–69)), suggesting that major evolutionary divergences may occur when neuronal identity is specified after cell-cycle exit. In line with this, the transcriptomes of radial glia and IPCs are highly correlated in mouse and salamander, but correlations drop once immature and mature neurons are compared (**Fig. 6A**). In salamander, hundreds of genes were differentially expressed along pseudotime in the differentiation trajectories leading to superficial- and deep-layer neurons (**Fig. 6B**). Differentially expressed genes at the split between superficial- and deep-layer trajectories included several transcription factors, such as *Foxp1* (a transcription factor specifying early-born neurons in the mammalian neocortex (70)) and *Pou3f1* in the superficial-layer trajectory and *Nr3c2*, *Nfix*, *Nfic*, *Zfpm2*, and *St18* in the deep-layer trajectory (**Fig. 6B-D**). We then compared these trajectory genes with the genes expressed at the first branch-point during mouse neocortical development, which corresponds to the split between intratelencephalic (IT)-projecting and non-IT projecting neurons (53, 69) (**Fig. 6C**). Strikingly, none of the top TFs differentially expressed at the salamander superficial- and deep-layer branch-point showed differential expression at the mouse IT vs non-IT branchpoint (**Fig. 6D**). Moreover, we found that the top TFs distinguishing mouse IT and non-IT trajectories were not differentially expressed in salamander superficial and deep-layer trajectories (**Fig. 6E**). This comparison demonstrates that neurons are specified by different gene regulatory programs in

the salamander dorsal pallium and mammalian neocortex, suggesting that evolutionary changes late in pallial development produce divergent neuron types in these two brain regions (29).

Neuronal identity is defined by the expression of distinct gene modules, each linked to a specific aspect of the neuron's phenotype or function. Some, but not all gene modules identified in the developing mouse neocortex (69) were also expressed in salamanders (**fig. S11**). We thus reasoned that salamander and mouse pallial neurons may still share some characteristics because of common features of their early development such as similar birthdates. To explore this possibility, we analyzed mouse neocortical subclasses (as defined by (71)) and tested whether genes differentially expressed between salamander early-born (superficial) and late-born (deep) neurons were sufficient to distinguish between early- and late-born neurons in the mouse. We further asked whether the same gene set could correctly classify mouse neocortical neurons based on their layer or projection identities (**Fig. 6F**). After training machine-learning classifiers (multinomial logistic regression models, see **Methods**) on these data, we assessed their ability to predict neuronal identity across these three axes: birthdate, layer, and projection. Surprisingly, the salamander superficial- and deep-layer specific genes were most effective at predicting projection identity in the mouse, followed by layer and then birthdate (**Fig. 6G**). Consistently, salamander superficial- and deep-layer genes showed enriched expression in mouse neurons with distinct projection identities: salamander superficial-layer markers were enriched in mouse extratelencephalic projection neurons not only in the neocortex, but also in the subiculum, postsubiculum, and retrosplenial cortex, while salamander deep-layer markers were enriched in mouse intratelencephalic-projecting neurons (**fig. S12**).

Tracing and single-cell dye filling experiments in several amphibian species indicate that dorsal pallium neurons are primarily intratelencephalic projection neurons (27, 72–74). Prompted by the enrichment of salamander superficial-layer neuron markers in mouse extratelencephalic projection neurons, we performed iontophoretic injections of the bidirectional tracer Neurobiotin in the diencephalon of adult salamanders, to verify the existence of pallial neurons projecting to extratelencephalic regions. Retrogradely-labeled cell bodies were detected in several telencephalic regions, with cell bodies in the dorsal and medial pallium mostly restricted to the superficial layer (**Fig. 6H-K**). Given that superficial-layer neurons are a small fraction of all DP neurons, it is likely they were missed in previous studies, which document only intratelencephalic projections from DP (27, 29, 72–74). Together, these data indicate that salamander superficial- and deep-layer neurons largely correspond to extra- and intratelencephalic projection neurons, respectively. In summary, our results show that neuronal birthdate, laminar position, molecular identity, and projection type are tightly linked in the salamander dorsal pallium, just as they are in the mammalian cerebral cortex, revealing a shared developmental logic underlying circuit assembly in both regions (**Fig. 6L**).

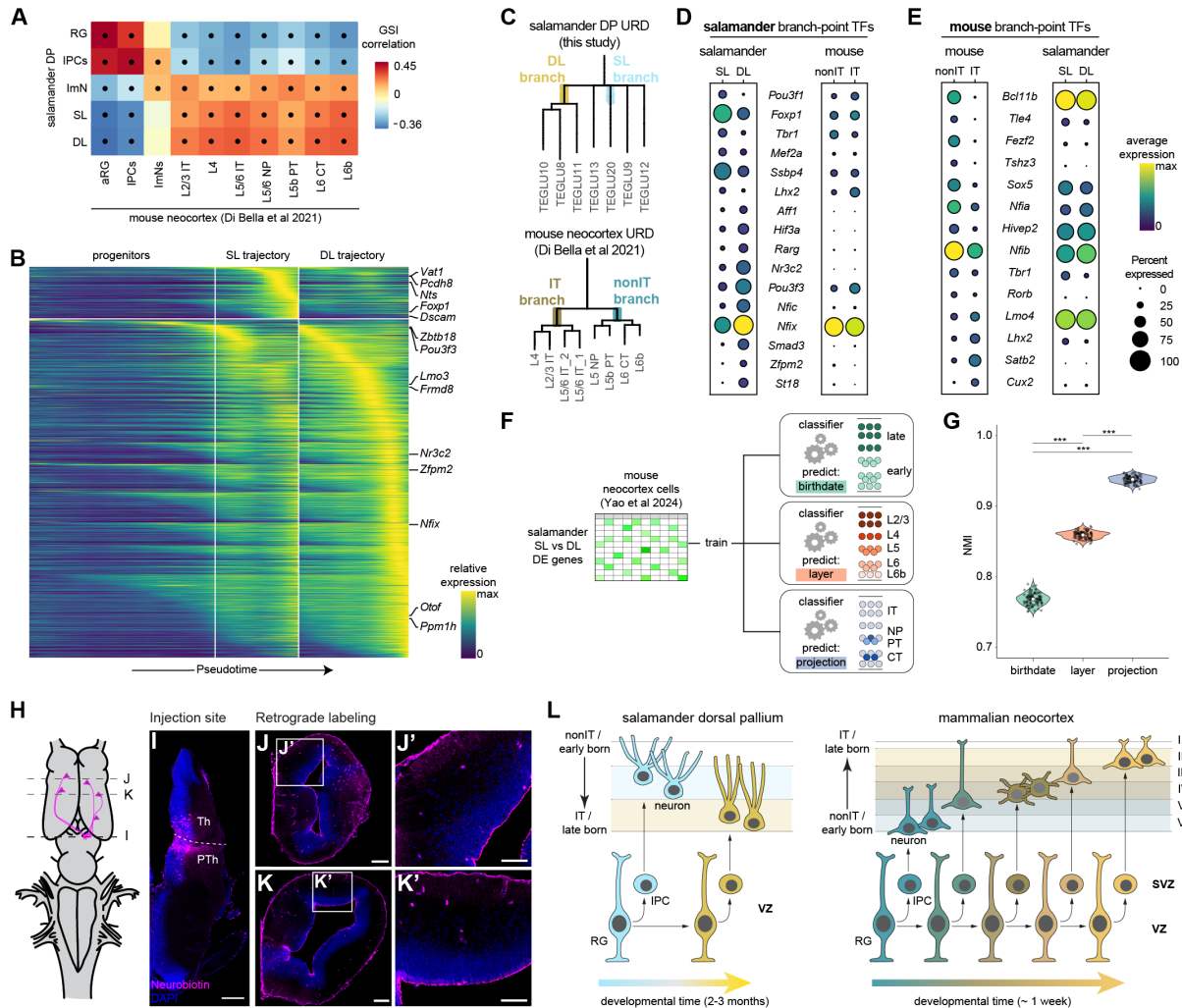


Fig. 6. Diverging differentiation programs after cell cycle exit produce conserved classes of pallial projection neurons. (A) Gene specificity index correlation matrix of cell types during salamander and mouse neurogenesis showing higher molecular correlations among progenitors, and lower correlations after cell-cycle exit. Dots indicate statistical significance ($p < 0.05$). Mouse data from (53). (B) Smoothed heatmap of gene expression in salamander dorsal pallium cell trajectories (fig. S10A), showing DE genes between SL and DL trajectories. (C) URD tree of salamander DP and mouse neocortex (from (53)), highlighting branches used for analysis in D,E. (D) Left: dotplot of top transcription factors differentially expressed at the URD branchpoint splitting salamander DL and SL neurons indicated in C. Right: expression of the same transcription factors in mouse. (E) Left: dotplot of top transcription factors differentially expressed at the URD branchpoint splitting mouse IT and non-IT neurons indicated in C. Right: expression of the same transcription factors in salamander. (F) Machine learning classifiers (multinomial logistic regression) were trained to predict alternative classification schemes of mouse neocortical types (birthdate, layer, projection) using only genes differentially expressed across salamander layers. (G) Normalized mutual information (NMI) score for each classifier after bootstrapping (NMI=0 indicates no agreement between predictions and ground truth, NMI=1 indicates perfect agreement). p values computed after a Kruskal-Wallis rank sum test and pairwise post-hoc comparisons with Dunn's test (***) $p \leq 0.001$. (H-K) Retrograde tracing schematic (H), visualization of the injection site in the thalamus/prethalamus (I) and retrogradely traced cells in the DP (J,K). Magnifications show labeled SL neurons in the DP. Scale bars in overview 200 μ m, in magnifications 100 μ m. (L) Comparison of neurogenesis in the salamander DP and mouse neocortex. Colors indicate birthdate, cellular morphologies represent divergence of cell identities, and are based on (23, 74).

Abbreviations: aRG, apical radial glia; CT, corticothalamic; DE, differentially expressed; DL, deep layer neurons; DP, dorsal pallium; GSI, gene specificity index; ImN, immature neurons; IPC, intermediate progenitor cell; IT, intratelencephalic; L, layer; NP, near-projecting; NMI, normalized mutual information; PT, pyramidal tract; PTh, prethalamus; RG, radial glia; SL, superficial layer neurons; SVZ, subventricular zone; TEGLU, telencephalic glutamatergic neurons; TFs transcription factors; Th, thalamus; VZ, ventricular zone.

Discussion

365 In this work, we characterized the cellular and molecular processes underlying the development of the amphibian dorsal pallium at single-cell resolution. Placed in a comparative context, our findings overturn longstanding assumptions about the evolution of cortical development. We identify conserved principles of corticogenesis, and clarify the series of developmental innovations that led to the emergence of a six-layered neocortex in mammals (**Fig. 6L**).

370 A central principle of mammalian cortical development is the sequential generation of distinct neuron types over time: the tight association of neuronal birthdate with molecular identity, laminar position, and projection pattern (reviewed in (36)). This is the case not only in the neocortex, but also in the hippocampus and piriform cortex, where neurons with different birthdates settle into distinct sublayers and exhibit distinct transcriptomes, connectivity, and function (10, 11, 14, 35). Here, we show that the salamander dorsal pallium is built following the same logic, in which two layers are generated through temporally patterned neurogenesis. Although the link between birthdate and molecular identity has not been directly demonstrated in other non-mammalian species, available data suggest that this principle may extend across vertebrates. Studies in turtles, lizards, frogs, and zebrafish have shown that pallial neurons born at different developmental times are arranged into a gradient along the radial axis (8, 75–78). In the gecko (5), alligator (9), and turtle (13) dorsal cortex, superficial and deep neurons have distinct gene expression profiles. Notably, in the turtle dorsal cortex, superficial neurons are early-born and extratelencephalic-projecting, whereas deep-layer neurons are late-born and intratelencephalic-projecting (8), resembling the salamander dorsal pallium. Indeed, superficial and deep layers have similar transcriptomes across these two species (29), suggesting that these layers are homologous and were present in tetrapod ancestors. To date, no evidence in fish directly indicates a link between neuronal birthdate, transcriptomic identities, and projections. However, zebrafish early-born pallial neurons congregate into a nucleus (Dc) that has a distinct transcriptomic identity (79); these neurons are extratelencephalic projecting, whereas late-born neurons are mostly intratelencephalic types (75). These observations suggest that the dichotomy between early-born and late-born neuronal identities may extend to vertebrate ancestors.

A second conserved feature of cortical development is the generation of multiple glutamatergic types by multipotent radial glia progenitors. In the neocortex, this is the foundation of the radial unit hypothesis (80). Hippocampal radial glia progenitors are also believed to be multipotent and generate spatially-clustered clones (32). Using TrackerSeq, we find that the same principle holds true in salamanders. Similarities between salamander and mouse extend to the molecular level: a conserved set of genes distinguishes early and late radial glia cells in both species. This finding points to the evolutionary conservation of a mechanism of cortical development: the temporal patterning of neural progenitors in the pallium across tetrapods. Furthermore, because the number of radial glia temporal states and the total number of neuron types and layers generated are not directly correlated, the evolution of a complex cell type repertoire in the

mammalian cortex was unlikely to have occurred through changes of temporal patterning. This contrasts with insects, where neuroblasts exist in discrete transcriptional states over time and
405 the diversification of these temporal states may be necessary for the evolution of new neuron types (81). Finally, we find that these conserved radial glia states do not track absolute time, but relative time. In salamanders, pallial neurogenesis spans 2-3 months, while in mice it lasts only about a week. This points to the existence of global mechanisms that align and scale the *tempo* of neurogenesis to the development of the rest of the organism.

410 A third conserved principle of cortical development is the deployment of two progenitor types: radial glia and intermediate progenitor cells. While the evolutionary conservation of radial glia cells is well established, the evolution of IPCs remains heavily debated (82). In the mammalian neocortex, IPCs delaminate from the ventricular surface and aggregate in a distinct band of cells called the subventricular zone (SVZ), where they divide and produce neurons (49, 64). With the
415 identification of an SVZ in the pallium of turtles and birds, it has been proposed that IPCs are an amniote innovation supporting the generation of large pallia, particularly in birds and mammals. Challenging this view, a Tbr2+ (*Eomes*) expressing SVZ was discovered in the shark pallium (83, 84). Scattered non-ventricular mitoses have also been reported in amphibians, but *Eomes*/Tbr2 expression in these putative IPCs could not be confirmed (77, 85). Our
420 transcriptomic analysis solves this conundrum by demonstrating that salamander *Eomes*+ progenitors express the battery of genes that defines mammalian IPCs, in line with recent results in chicken (86) and sharks (87). These cells are mitotic and committed to a neuronal fate, suggesting the presence of indirect neurogenesis. Together, these data indicate that *Eomes*-expressing IPCs existed in the pallium of jawed vertebrate ancestors, most likely to increase the
425 neuronal output of radial glia cells. The flexible deployment of this progenitor type, culminating with their delamination into an SVZ multiple times independently across vertebrates, may have enabled the expansion of selected pallial regions without fundamental modifications of radial glia progenitors. Indeed, changes of Notch/Delta and Slit/Robo signaling levels are sufficient to shift the abundance and proliferative behavior of IPCs (49), suggesting a potential mechanism for the
430 differential recruitment of this progenitor type in vertebrates.

Besides these conserved principles, our analysis in salamanders also clarifies what innovations of cortical development may have led to the evolution of complex cerebral cortices in mammals. We show that, while early steps of corticogenesis rely on conserved progenitor types, the differentiation cascades that unfold after cell cycle exit differ markedly in mouse and
435 salamander. We propose that the evolutionary divergence of neuronal differentiation programs was instrumental for the increase of neuronal diversity and of layers in mammals - although we cannot fully rule out that these differentiation programs stem from subtle molecular heterogeneities in radial glia or IPCs. This divergence is so profound that prior transcriptomic comparisons of adult pallial neurons could not identify clear one-to-one homologies across
440 species (13, 29, 51). Our study, however, shows that early- and late-born neurons in amphibians and mammals have shared transcriptomic signatures and similar projection targets, resonating

with data from reptiles (13). We thus propose that neuronal birthdates identify two ancestral classes of pyramidal neurons - extra-telencephalic and intra-telencephalic projection neurons - and that diversification within each of these classes produced the plethora of neuron types that
445 populate not only the mammalian neocortex, but also adjacent areas such as the entorhinal cortex and the subicular complex (29).

A second striking difference across species is the distribution of neurons with different birthdates along the radial axis: outside-in (early-born neurons in superficial layers, late-born neurons in deep) in non-mammals as opposed to inside-out (early-born neurons in deep layers, late-born
450 neurons in superficial) in mammals (**Fig. 6L**). Outside-in neurogenesis has been documented in the pallium of turtles (8, 76), lizards (78), frogs (77), and fish (75, 88). Changes in Wnt signaling in immature neurons may have enabled later-born neurons to migrate past earlier-born neurons, thus facilitating the emergence of a mammalian-specific mode of radial migration (89). Cajal-Retzius cells, which in mammals regulate radial migration through Reelin signaling, are present
455 in non-mammalian species, but their increased abundance and higher *Reelin* expression in the mammalian pallium may have also contributed to the emergence of radial migration (90). It has been suggested that the inversion of the corticogenesis gradient enabled late-born neurons to gain access to thalamic inputs, which in non-mammals reach the cortex through a superficial path (91). This change, together with the emergence of a new thalamocortical route (92), may
460 have relieved constraints for the further diversification of late-born cortico-cortical projection neurons, supporting the further expansion and specialization of the cerebral cortex in mammalian ancestors.

References

- 465 1. G. F. Striedter, R. G. Northcutt, G. F. Striedter, R. G. Northcutt, *Brains Through Time: A Natural History of Vertebrates* (Oxford University Press, Oxford, New York, 2020).
2. R. Glenn Northcutt, J. H. Kaas, The emergence and evolution of mammalian neocortex. *Trends Neurosci.* **18**, 373–379 (1995).
3. L. Medina, A. Reiner, Do birds possess homologues of mammalian primary visual,
470 somatosensory and motor cortices? *Trends Neurosci.* **23**, 1–12 (2000).
4. M. Stacho, C. Herold, N. Rook, H. Wagner, M. Axer, K. Amunts, O. Güntürkün, A cortex-like canonical circuit in the avian forebrain. *Science* **369** (2020).
5. E. Rueda-Alaña, R. Senovilla-Ganzo, M. Grillo, E. Vázquez, S. Marco-Salas, T. Gallego-Flores, A. Ordeñana-Manso, A. Ftara, L. Escobar, A. Benguría, A. Quintas, A. Dopazo, M.
475 Rábano, M. dM Vivanco, A. M. Aransay, D. Garrigos, Á. Toval, J. L. Ferrán, M. Nilsson, J. M. Encinas-Pérez, M. De Pittà, F. García-Moreno, Evolutionary convergence of sensory circuits in the pallium of amniotes. *Science* **387**, eadp3411 (2025).
6. L. Puelles, A. Alonso, E. García-Calero, M. Martínez-de-la-Torre, Concentric ring topology

- of mammalian cortical sectors and relevance for patterning studies. *J. Comp. Neurol.* **527**, 1731–1752 (2019).
- 480
7. R. K. Naumann, G. Laurent, “1.25 - Function and Evolution of the Reptilian Cerebral Cortex” in *Evolution of Nervous Systems (Second Edition)*, J. H. Kaas, Ed. (Academic Press, Oxford, 2017); <https://www.sciencedirect.com/science/article/pii/B9780128040423000221>), pp. 491–518.
- 485
8. M. G. Blanton, A. R. Kriegstein, Morphological differentiation of distinct neuronal classes in embryonic turtle cerebral cortex. *J. Comp. Neurol.* **310**, 550–570 (1991).
9. S. D. Briscoe, C. W. Ragsdale, Molecular anatomy of the alligator dorsal telencephalon. *J. Comp. Neurol.* **526**, 1613–1646 (2018).
10. R. Cossart, R. Khazipov, How development sculpts hippocampal circuits and function. *Physiol. Rev.* **102**, 343–378 (2022).
- 490
11. A. Diodato, M. Ruinat de Brimont, Y. S. Yim, N. Derian, S. Perrin, J. Pouch, D. Klatzmann, S. Garel, G. B. Choi, A. Fleischmann, Molecular signatures of neural connectivity in the olfactory cortex. *Nat. Commun.* **7**, 12238 (2016).
12. L. Slomianka, I. Amrein, I. Knuesel, J. C. Sørensen, D. P. Wolfer, Hippocampal pyramidal cells: the reemergence of cortical lamination. *Brain Struct. Funct.* **216**, 301–317 (2011).
- 495
13. M. A. Tosches, T. M. Yamawaki, R. K. Naumann, A. A. Jacobi, G. Tushev, G. Laurent, Evolution of pallium, hippocampus, and cortical cell types revealed by single-cell transcriptomics in reptiles. *Science* **360**, 881–888 (2018).
14. S. Zeppilli, A. O. Gurrola, P. Demetci, D. H. Brann, T. M. Pham, R. Attey, N. Zilkha, T. Kimchi, S. R. Datta, R. Singh, M. A. Tosches, A. Crombach, A. Fleischmann, Single-cell genomics of the mouse olfactory cortex reveals contrasts with neocortex and ancestral signatures of cell type evolution. *Nat. Neurosci.* **28**, 937–948 (2025).
- 500
15. J. Fournier, C. M. Müller, G. Laurent, Looking for the roots of cortical sensory computation in three-layered cortices. *Curr. Opin. Neurobiol.* **31**, 119–126 (2015).
- 505
16. L. B. Haberly, J. M. Bower, Olfactory cortex: model circuit for study of associative memory? *Trends Neurosci.* **12**, 258–264 (1989).
17. M. Larkum, A cellular mechanism for cortical associations: an organizing principle for the cerebral cortex. *Trends Neurosci.* **36**, 141–151 (2013).
18. G. M. Shepherd, T. B. Rowe, Neocortical Lamination: Insights from Neuron Types and Evolutionary Precursors. *Front. Neuroanat.* **11** (2017).
- 510
19. M. E. Larkum, L. S. Petro, R. N. S. Sachdev, L. Muckli, A Perspective on Cortical Layering and Layer-Spanning Neuronal Elements. *Front. Neuroanat.* **12** (2018).
20. D. B. Chklovskii, T. Schikorski, C. F. Stevens, Wiring Optimization in Cortical Circuits.

- Neuron* **34**, 341–347 (2002).
- 515 21. R. J. Douglas, K. A. C. Martin, Neuronal circuits of the neocortex. *Annu. Rev. Neurosci.* **27**, 419–451 (2004).
22. J. Guy, J. F. Staiger, The functioning of a cortex without layers. *Front. Neuroanat.* **11**, 1–13 (2017).
23. K. D. Harris, G. M. G. Shepherd, The neocortical circuit: Themes and variations. *Nat. Neurosci.* **18**, 170–181 (2015).
- 520 24. Northcutt, Elasmobranch Central Nervous System Organization and Its Possible Evolutionary Significance. *Am. Zool.* **17**, 411–429 (1977).
25. R. G. Northcutt, E. Kicliter, Organization of the Amphibian Telencephalon. *Comp. Neurol. Telencephalon*, 203–255 (1980).
- 525 26. S. M. Suryanarayana, B. Robertson, P. Wallén, S. Grillner, The Lamprey Pallium Provides a Blueprint of the Mammalian Layered Cortex. *Curr. Biol.* **27**, 3264–3277.e5 (2017).
27. T. J. Neary, “The Pallium of Anuran Amphibians” in *Comparative Structure and Evolution of Cerebral Cortex, Part I* (1990)vol. SA, pp. 107–138.
28. R. Nieuwenhuys, H. J. Donkelaar, C. Nicholson in *The Central Nervous System of Vertebrates* (Springer Berlin, 1998), p. 1933.
- 530 29. J. Woych, A. Ortega Gurrola, A. Deryckere, E. C. B. Jaeger, E. Gumnit, G. Merello, J. Gu, A. Joven Araus, N. D. Leigh, M. Yun, A. Simon, M. A. Tosches, Cell-type profiling in salamanders identifies innovations in vertebrate forebrain evolution. *Science* **377**, eabp9186 (2022).
- 535 30. R. Beattie, S. Hippenmeyer, Mechanisms of radial glia progenitor cell lineage progression. *FEBS Lett.* **591**, 3993–4008 (2017).
31. D. Huilgol, J. B. Russ, S. Srivas, Z. J. Huang, The progenitor basis of cortical projection neuron diversity. *Curr. Opin. Neurobiol.* **81**, 102726 (2023).
32. H. T. Xu, Z. Han, P. Gao, S. He, Z. Li, W. Shi, O. Kodish, W. Shao, K. N. Brown, K. Huang, S. H. Shi, Distinct lineage-dependent structural and functional organization of the hippocampus. *Cell* **157**, 1552–1564 (2014).
- 540 33. G. Cheung, F. M. Pauler, P. Koppensteiner, T. Krausgruber, C. Streicher, M. Schrammel, N. Gutmann-Özgen, A. E. Ivec, C. Bock, R. Shigemoto, S. Hippenmeyer, Multipotent progenitors instruct ontogeny of the superior colliculus. *Neuron* **112**, 230–246.e11 (2024).
- 545 34. M. Rahimi-Balaei, H. Bergen, J. Kong, H. Marzban, Neuronal Migration During Development of the Cerebellum. *Front. Cell. Neurosci.* **12**, 484 (2018).
35. E. Klingler, Development and Organization of the Evolutionarily Conserved Three-

- Layered Olfactory Cortex. *eNeuro* **4** (2017).
36. K. Y. Kwan, N. Šestan, E. S. Anton, Transcriptional co-regulation of neuronal migration and laminar identity in the neocortex. *Development* **139**, 1535–1546 (2012).
550
37. B. J. Molyneaux, P. Arlotta, J. R. L. Menezes, J. D. Macklis, Neuronal subtype specification in the cerebral cortex. *Nat. Rev. Neurosci.* **8**, 427–437 (2007).
38. D. Cavalieri, A. Angelova, A. Islah, C. Lopez, M. Bocchio, Y. Bollmann, A. Baude, R. Cossart, CA1 pyramidal cell diversity is rooted in the time of neurogenesis. *eLife* **10**, e69270 (2021).
555
39. R. Huszár, Y. Zhang, H. Blockus, G. Buzsáki, Preconfigured dynamics in the hippocampus are guided by embryonic birthdate and rate of neurogenesis. *Nat. Neurosci.* **25**, 1201–1212 (2022).
40. V. A. Kveim, L. Salm, T. Ulmer, M. Lahr, S. Kandler, F. Imhof, F. Donato, Divergent recruitment of developmentally defined neuronal ensembles supports memory dynamics. *Science* **385**, eadk0997 (2024).
560
41. T. Monko, J. Rebertus, J. Stolley, S. R. Salton, Y. Nakagawa, Thalamocortical axons regulate neurogenesis and laminar fates in the early sensory cortex. *Proc. Natl. Acad. Sci.* **119**, e2201355119 (2022).
- 565 42. A. Deryckere, J. Woych, E. C. B. Jaeger, M. A. Tosches, Molecular Diversity of Neuron Types in the Salamander Amygdala and Implications for Amygdalar Evolution. *Brain. Behav. Evol.* **98**, 61–75 (2023).
43. A. Joven, R. Morona, N. Moreno, A. González, Regional distribution of calretinin and calbindin-D28k expression in the brain of the urodele amphibian *Pleurodeles waltl* during embryonic and larval development. *Brain Struct. Funct.* **218**, 969–1003 (2013).
570
44. A. Joven, H. Wang, T. Pinheiro, L. S. Hameed, L. Belnoue, A. Simon, Cellular basis of brain maturation and acquisition of complex behaviors in salamanders. *Development* **145** (2018).
- 575 45. E. C. B. Jaeger, D. Vijatovic, A. Deryckere, N. Zorin, A. L. Nguyen, G. Ivanian, J. Woych, R. C. Arnold, A. O. Gurrola, A. Shvartsman, F. Barbieri, F. A. Toma, H. T. Cline, T. F. Shay, D. B. Kelley, A. Yamaguchi, M. Shein-Idelson, M. A. Tosches, L. B. Sweeney, Adeno-associated viral tools to trace neural development and connectivity across amphibians. *Dev. Cell* **60**, 794–812 (2025).
- 580 46. R. C. Bandler, I. Vitali, R. N. Delgado, M. C. Ho, E. Dvoretzkova, J. S. Ibarra Molinas, P. W. Frazel, M. Mohammadkhani, R. Machold, S. Maedler, S. A. Liddelow, T. J. Nowakowski, G. Fishell, C. Mayer, Single-cell delineation of lineage and genetic identity in the mouse brain. *Nature* **601**, 404–409 (2022).
47. D. E. Wagner, C. Weinreb, Z. M. Collins, J. A. Briggs, S. G. Megason, A. M. Klein, Single-

- cell mapping of gene expression landscapes and lineage in the zebrafish embryo.
585 *Science* **360**, 981–987 (2018).
48. S. A. Bayer, J. Altman, Development of the endopiriform nucleus and the claustrum in the rat brain. *Neuroscience* **45**, 391–412 (1991).
49. A. Cárdenas, A. Villalba, C. de Juan Romero, E. Picó, C. Kyrousi, A. C. Tzika, M. Tessier-Lavigne, L. Ma, M. Drukker, S. Cappello, V. Borrell, Evolution of Cortical Neurogenesis in Amniotes Controlled by Robo Signaling Levels. *Cell* **174**, 590-606.e21 (2018).
590
50. L. Telley, G. Agirman, J. Prados, N. Amberg, S. Fièvre, P. Oberst, G. Bartolini, I. Vitali, C. Cadilhac, S. Hippenmeyer, L. Nguyen, A. Dayer, D. Jabaudon, Temporal patterning of apical progenitors and their daughter neurons in the developing neocortex. *Science* **364** (2019).
- 595 51. K. Lust, A. Maynard, T. Gomes, J. S. Fleck, J. G. Camp, E. M. Tanaka, B. Treutlein, Single-cell analyses of axolotl telencephalon organization, neurogenesis, and regeneration. *Science* **377**, eabp9262 (2022).
52. X. Wei, S. Fu, H. Li, Y. Liu, S. Wang, W. Feng, Y. Yang, X. Liu, Y. Y. Zeng, M. Cheng, Y. Lai, X. Qiu, L. Wu, N. Zhang, Y. Jiang, J. Xu, X. Su, C. Peng, L. Han, W. P. K. Lou, C. Liu, Y. Yuan, K. Ma, T. Yang, X. Pan, S. Gao, A. Chen, M. A. Esteban, H. Yang, J. Wang, G. Fan, L. Liu, L. Chen, X. Xu, J. F. Fei, Y. Gu, Single-cell Stereo-seq reveals induced progenitor cells involved in axolotl brain regeneration. *Science* **377**, eabp9444 (2022).
600
53. D. J. Di Bella, E. Habibi, R. R. Stickels, G. Scalia, J. Brown, P. Yadollahpour, S. M. Yang, C. Abbate, T. Biancalani, E. Z. Macosko, F. Chen, A. Regev, P. Arlotta, Molecular logic of cellular diversification in the mouse cerebral cortex. *Nature* **595**, 554–559 (2021).
605
54. A. R. Bright, Y. Kotlyarenko, F. Neuhaus, D. Rodrigues, C. Feng, C. Peters, I. Vitali, E. Dönmez, M. H. Myoga, E. Dvoretzkova, C. Mayer, Temporal control of progenitor competence shapes maturation in GABAergic neuron development in mice. *Nat. Neurosci.* **28**, 1663–1675 (2025).
- 610 55. P. Lyu, T. Hoang, C. P. Santiago, E. D. Thomas, A. E. Timms, H. Appel, M. Gimmen, N. Le, L. Jiang, D. W. Kim, S. Chen, D. F. Espinoza, A. E. Telger, K. Weir, B. S. Clark, T. J. Cherry, J. Qian, S. Blackshaw, Gene regulatory networks controlling temporal patterning, neurogenesis, and cell-fate specification in mammalian retina. *Cell Rep.* **37**, 109994 (2021).
- 615 56. C. C. A. Mannens, L. Hu, P. Lönnerberg, M. Schipper, C. C. Reagor, X. Li, X. He, R. A. Barker, E. Sundström, D. Posthuma, S. Linnarsson, Chromatin accessibility during human first-trimester neurodevelopment. *Nature*, 1–8 (2024).
57. X. Ruan, B. Kang, C. Qi, W. Lin, J. Wang, X. Zhang, Progenitor cell diversity in the developing mouse neocortex. *Proc. Natl. Acad. Sci.* **118**, 1–8 (2021).

- 620 58. A. Sagner, I. Zhang, T. Watson, J. Lazaro, M. Melchionda, J. Briscoe, A shared transcriptional code orchestrates temporal patterning of the central nervous system. *PLOS Biol.* **19**, e3001450 (2021).
59. A. B. Tonchev, T. C. Tuoc, E. H. Rosenthal, M. Studer, A. Stoykova, Zbtb20 modulates the sequential generation of neuronal layers in developing cortex. *Mol. Brain* **9**, 65 (2016).
- 625 60. J. A. Farrell, Y. Wang, S. J. Riesenfeld, K. Shekhar, A. Regev, A. F. Schier, Single-cell reconstruction of developmental trajectories during zebrafish embryogenesis. *Science* **360**, eaar3131 (2018).
61. E. Braun, M. Danan-Gotthold, L. E. Borm, K. W. Lee, E. Vinsland, P. Lönnerberg, L. Hu, X. Li, X. He, Ž. Andrusivová, J. Lundeberg, R. A. Barker, E. Arenas, E. Sundström, S. Linnarsson, Comprehensive cell atlas of the first-trimester developing human brain. *Science* **382**, eadf1226 (2023).
- 630 62. R. F. Hevner, Intermediate progenitors and Tbr2 in cortical development. *J. Anat.* **235**, 616–625 (2019).
63. A. Cárdenas, V. Borrell, Molecular and cellular evolution of corticogenesis in amniotes. *Cell. Mol. Life Sci.* **77**, 1435–1460 (2020).
- 635 64. A. F. P. Cheung, S. Kondo, O. Abdel-Mannan, R. A. Chodroff, T. M. Sirey, L. E. Bluy, N. Webber, J. DeProto, S. J. Karlen, L. Krubitzer, H. B. Stolp, N. R. Saunders, Z. Molnár, The Subventricular Zone Is the Developmental Milestone of a 6-Layered Neocortex: Comparisons in Metatherian and Eutherian Mammals. *Cereb. Cortex* **20**, 1071–1081 (2010).
- 640 65. A. Kriegstein, S. Noctor, V. Martínez-Cerdeño, Patterns of neural stem and progenitor cell division may underlie evolutionary cortical expansion. *Nat. Rev. Neurosci.* **7**, 883–890 (2006).
66. M. X. Moreau, Y. Saillour, A. W. Cwetsch, A. Pierani, F. Causeret, Single-cell transcriptomics of the early developing mouse cerebral cortex disentangle the spatial and temporal components of neuronal fate acquisition. *Dev. Camb.* **148** (2021).
- 645 67. N. Baumann, I. Morassut, S. Roig-Puiggros, E. Klingler, G. Bartolini, S. Fièvre, D. Jabaudon, Cell-extrinsic controls over neocortical neuron fate and diversity. *Sci. Adv.* **11**, eadw0218 (2025).
- 650 68. L. Del-Valle-Anton, S. Amin, D. Cimino, F. Neuhaus, E. Dvoretzkova, V. Fernández, Y. K. Babal, C. Garcia-Frigola, A. Prieto-Colomina, R. Murcia-Ramón, Y. Nomura, A. Cárdenas, C. Feng, J. A. Moreno-Bravo, M. Götz, C. Mayer, V. Borrell, Multiple parallel cell lineages in the developing mammalian cerebral cortex. *Sci. Adv.* **10**, eadn9998 (2024).
- 655 69. Y. Gao, C. T. J. van Velthoven, C. Lee, E. D. Thomas, D. Bertagnolli, D. Carey, T. Casper, A. B. Chakka, R. Chakrabarty, M. Clark, M. J. Desierto, R. Ferrer, J. Gloe, J.

- 660 Goldy, N. Guilford, J. Guzman, C. R. Halterman, D. Hirschstein, W. Ho, K. James, R. McCue, E. Meyerdierks, B. Nguy, N. Pena, T. Pham, N. V. Shapovalova, J. Sulc, A. Torkelson, A. Tran, H. Tung, J. Wang, K. Ronellenfitch, B. Levi, M. J. Hawrylycz, C. Pagan, N. Dee, K. A. Smith, B. Tasic, Z. Yao, H. Zeng, Continuous cell type diversification throughout the embryonic and postnatal mouse visual cortex development. [Preprint] (2024). <https://doi.org/10.1101/2024.10.02.616246>.
70. C. A. Pearson, D. M. Moore, H. O. Tucker, J. D. Dekker, H. Hu, A. Miquelajáuregui, B. G. Novitch, *Foxp1* Regulates Neural Stem Cell Self-Renewal and Bias Toward Deep Layer Cortical Fates. *Cell Rep.* **30**, 1964-1981.e3 (2020).
- 665 71. Z. Yao, C. T. J. van Velthoven, M. Kunst, M. Zhang, D. McMillen, C. Lee, W. Jung, J. Goldy, A. Abdelhak, M. Aitken, K. Baker, P. Baker, E. Barkan, D. Bertagnolli, A. Bhandiwad, C. Bielstein, P. Bishwakarma, J. Campos, D. Carey, T. Casper, A. B. Chakka, R. Chakrabarty, S. Chavan, M. Chen, M. Clark, J. Close, K. Crichton, S. Daniel, P. DiValentin, T. Dolbeare, L. Ellingwood, E. Fiabane, T. Fliss, J. Gee, J. Gerstenberger, A. 670 Glandon, J. Gloe, J. Gould, J. Gray, N. Guilford, J. Guzman, D. Hirschstein, W. Ho, M. Hooper, M. Huang, M. Hupp, K. Jin, M. Kroll, K. Lathia, A. Leon, S. Li, B. Long, Z. Madigan, J. Malloy, J. Malone, Z. Maltzer, N. Martin, R. McCue, R. McGinty, N. Mei, J. Melchor, E. Meyerdierks, T. Mollenkopf, S. Moonsman, T. N. Nguyen, S. Otto, T. Pham, C. Rimorin, A. Ruiz, R. Sanchez, L. Sawyer, N. Shapovalova, N. Shepard, C. 675 Slaughterbeck, J. Sulc, M. Tieu, A. Torkelson, H. Tung, N. Valera Cuevas, S. Vance, K. Wadhvani, K. Ward, B. Levi, C. Farrell, R. Young, B. Staats, M.-Q. M. Wang, C. L. Thompson, S. Mufti, C. M. Pagan, L. Kruse, N. Dee, S. M. Sunkin, L. Esposito, M. J. Hawrylycz, J. Waters, L. Ng, K. Smith, B. Tasic, X. Zhuang, H. Zeng, A high-resolution transcriptomic and spatial atlas of cell types in the whole mouse brain. *Nature* **624**, 317–332 (2023). 680
72. G. Roth, F. Laberge, S. Mühlenbrock-Lenter, W. Grunwald, Organization of the pallium in the fire-bellied toad *Bombina orientalis*. I: Morphology and axonal projection pattern of neurons revealed by intracellular biocytin labeling. *J. Comp. Neurol.* **501**, 443–464 (2007).
73. M. Sassoe, C. Pairault, P. Clairambault, A. Fasolo, The connections of the anterior 685 pallium in *Pleurodeles waltl* and *Triturus carnifex*: An HRP study. *J. Hirnforsch.* **32**, 397–407 (1991).
74. G. Westhoff, G. Roth, Morphology and projection pattern of medial and dorsal pallial neurons in the frog *Discoglossus pictus* and the salamander *Plethodon jordani*. *J. Comp. Neurol.* **445**, 97–121 (2002).
- 690 75. G. Furlan, V. Cuccioli, N. Vuillemin, L. Dirian, A. J. Muntasell, M. Coolen, N. Dray, S. Bedu, C. Houart, E. Beaurepaire, I. Foucher, L. Bally-Cuif, Life-Long Neurogenic Activity of Individual Neural Stem Cells and Continuous Growth Establish an Outside-In Architecture in the Teleost Pallium. *Curr. Biol.* **27**, 3288-3301.e3 (2017).

- 695 76. A. M. Goffinet, Ch. Daumerie, B. Langerwerf, C. Pieau, Neurogenesis in reptilian cortical structures: 3H-thymidine autoradiographic analysis. *J. Comp. Neurol.* **243**, 106–116 (1986).
77. N. Moreno, A. González, Pattern of neurogenesis and identification of neuronal progenitor subtypes during pallial development in *Xenopus laevis*. *Front. Neuroanat.* **11**, 1–24 (2017).
- 700 78. T. Nomura, H. Gotoh, K. Ono, Changes in the regulation of cortical neurogenesis contribute to encephalization during amniote brain evolution. *Nat. Commun.* **4** (2013).
79. L. Anneser, C. Satou, H.-R. Hotz, R. W. Friedrich, Molecular organization of neuronal cell types and neuromodulatory systems in the zebrafish telencephalon. *Curr. Biol.* **34**, 298–312.e4 (2024).
- 705 80. P. Rakic, Specification of Cerebral Cortical Areas. *Science* **241**, 170–176 (1988).
81. M. Perry, N. Konstantinides, F. Pinto-Teixeira, C. Desplan, Generation and Evolution of Neural Cell Types and Circuits: Insights from the Drosophila Visual System. *Annu. Rev. Genet.* **51**, 501–527 (2017).
- 710 82. R. F. Hevner, “Intermediate Progenitors in Neocortical Development and Evolution” in *Neocortical Neurogenesis in Development and Evolution* (John Wiley & Sons, Ltd, 2023; <https://onlinelibrary.wiley.com/doi/abs/10.1002/9781119860914.ch3>), pp. 41–61.
83. A. Docampo-Seara, R. Lagadec, S. Mazan, M. A. Rodríguez, I. Quintana-Urzainqui, E. Candal, Study of pallial neurogenesis in shark embryos and the evolutionary origin of the subventricular zone. *Brain Struct. Funct.* **223**, 3593–3612 (2018).
- 715 84. A. Docampo-Seara, S. Pereira-Guldrís, N. Sánchez-Farías, S. Mazan, M. A. Rodríguez, E. Candal, Characterization of neurogenic niches in the telencephalon of juvenile and adult sharks. *Brain Struct. Funct.* **225**, 817–839 (2020).
- 720 85. T. Nomura, C. Ohtaka-Maruyama, W. Yamashita, Y. Wakamatsu, Y. Murakami, F. Calegari, K. Suzuki, H. Gotoh, K. Ono, The evolution of basal progenitors in the developing non-mammalian brain. *Development* **143**, 66–74 (2016).
86. B. Zaremba, A. Fallahshahroudi, C. Schneider, J. Schmidt, I. Sarropoulos, E. Leushkin, B. Berki, E. Van Poucke, P. Jensen, R. Senovilla-Ganzo, F. Hervas-Sotomayor, N. Trost, F. Lamanna, M. Sepp, F. García-Moreno, H. Kaessmann, Developmental origins and evolution of pallial cell types and structures in birds. *Science* **387**, eadp5182 (2025).
- 725 87. I. Quintana-Urzainqui, T. Gerber, P. A. Oel, L. Pan, N. Papadopoulos, Z. G. Serka, A. Verbanac, M. Börsig, D. Torres-Sabino, I. C. Rollán-Delgado, L. Santangeli, H. Kaessmann, D. Arendt, An atlas of shark developing telencephalon reveals ancient origin of basal progenitors and Cajal-Retzius cells. bioRxiv [Preprint] (2025). <https://doi.org/10.1101/2025.05.08.652169>.

- 730 88. T. Foley, M. Thetiot, L. Bally-Cuif, Neural Stem Cell Regulation in Zebrafish. *Annu. Rev. Genet.* **58**, 249–272 (2024).
89. T. Nomura, C. Ohtaka-Maruyama, H. Kiyonari, H. Gotoh, K. Ono, Changes in Wnt-Dependent Neuronal Morphology Underlie the Anatomical Diversification of Neocortical Homologs in Amniotes. *Cell Rep.* **31**, 107592 (2020).
- 735 90. E. Gumnit, G. Gattoni, J. Woych, A. Deryckere, P. Bhattarai, J. A. Gillis, C. Kizil, M. A. Tosches, Evolution of Cajal-Retzius Cells in Vertebrates from an Ancient Class of Tp73+ Neurons. bioRxiv [Preprint] (2025). <https://doi.org/10.1101/2025.08.21.671508>.
91. F. Aboitiz, Feature Article: Evolution of Isocortical Organization. A Tentative Scenario Including Roles of Reelin, p35/cdk5 and the Subplate Zone. *Cereb. Cortex* **9**, 655–661 (1999).
- 740 92. F. Bielle, P. Marcos-Mondejar, M. Keita, C. Mailhes, C. Verney, K. Nguyen Ba-Charvet, M. Tessier-Lavigne, G. Lopez-Bendito, S. Garel, Slit2 Activity in the Migration of Guidepost Neurons Shapes Thalamic Projections during Development and Evolution. *Neuron* **69**, 1085–1098 (2011).
- 745 93. A. Joven, M. Kirkham, A. Simon, “Husbandry of Spanish Ribbed Newts (*Pleurodeles waltli*)” in *Salamanders in Regeneration Research: Methods and Protocols*, A. Kumar, A. Simon, Eds. (Springer, New York, NY, 2015; https://doi.org/10.1007/978-1-4939-2495-0_4), pp. 47–70.
94. L. Gallien, M. Durocher, Table chronologique du développement chez *Pleurodeles waltli* Michah. *Bull. Biol.* **2**, 1–19 (1957).
- 750 95. G. F. Alheid, “Small Injections of Axonally Transported Fluorescent Tracers” in *Methods in Neurosciences*, P. M. Conn, Ed. (Academic Press, 1990; <https://www.sciencedirect.com/science/article/pii/B9780121852559500213>)vol. 3 of *Quantitative and Qualitative Microscopy*, pp. 291–314.
- 755 96. E. Kuehn, D. S. Clausen, R. W. Null, B. M. Metzger, A. D. Willis, B. D. Özpolat, Segment number threshold determines juvenile onset of germline cluster expansion in *Platynereis dumerilii*. *J. Exp. Zool. B Mol. Dev. Evol.* **338**, 225–240 (2022).
97. J. S. Dasen, A. De Camilli, B. Wang, P. W. Tucker, T. M. Jessell, Hox Repertoires for Motor Neuron Diversity and Connectivity Gated by a Single Accessory Factor, FoxP1. *Cell* **134**, 304–316 (2008).
- 760 98. R. Patro, G. Duggal, M. I. Love, R. A. Irizarry, C. Kingsford, Salmon provides fast and bias-aware quantification of transcript expression. *Nat. Methods* **14**, 417–419 (2017).
99. Y. Hao, S. Hao, E. Andersen-Nissen, W. M. Mauck, S. Zheng, A. Butler, M. J. Lee, A. J. Wilk, C. Darby, M. Zager, P. Hoffman, M. Stoeckius, E. Papalexi, E. P. Mimitou, J. Jain, A. Srivastava, T. Stuart, L. M. Fleming, B. Yeung, A. J. Rogers, J. M. McElrath, C. A.
- 765

- Blish, R. Gottardo, P. Smibert, R. Satija, Integrated analysis of multimodal single-cell data. *Cell* **184**, 3573-3587.e29 (2021).
100. S. Choudhary, R. Satija, Comparison and evaluation of statistical error models for scRNA-seq. *Genome Biol.* **23**, 27 (2022).
- 770 101. C. Hafemeister, R. Satija, Normalization and variance stabilization of single-cell RNA-seq data using regularized negative binomial regression. *Genome Biol.* **20**, 296 (2019).
102. R. Cannoodt, H. Bengtsson, rcanoodt/princurve: princurve 2.1.4, version 2.1.4, Zenodo (2019); <https://doi.org/10.5281/zenodo.3351282>.
103. T. Hastie, W. and Stuetzle, Principal Curves. *J. Am. Stat. Assoc.* **84**, 502–516 (1989).
- 775 104. K. Van den Berge, H. Roux de Bézieux, K. Street, W. Saelens, R. Cannoodt, Y. Saeys, S. Dudoit, L. Clement, Trajectory-based differential expression analysis for single-cell sequencing data. *Nat. Commun.* **11**, 1201 (2020).
105. G. Yu, L.-G. Wang, Y. Han, Q.-Y. He, clusterProfiler: an R Package for Comparing Biological Themes Among Gene Clusters. *OMICS J. Integr. Biol.* **16**, 284–287 (2012).
- 780 106. B. Raj, J. A. Farrell, J. Liu, J. El Kholtei, A. N. Carte, J. Navajas Acedo, L. Y. Du, A. McKenna, Đ. Relić, J. M. Leslie, A. F. Schier, Emergence of Neuronal Diversity during Vertebrate Brain Development. *Neuron* **108**, 1058-1074.e6 (2020).
107. S. Aibar, C. B. González-Blas, T. Moerman, V. A. Huynh-Thu, H. Imrichova, G. Hulselmans, F. Rambow, J.-C. Marine, P. Geurts, J. Aerts, J. van den Oord, Z. K. Atak, J. Wouters, S. Aerts, SCENIC: single-cell regulatory network inference and clustering. *Nat. Methods* **14**, 1083–1086 (2017).
- 785 108. L. Zhao, Z. Liu, S. F. Levy, S. Wu, Bartender: a fast and accurate clustering algorithm to count barcode reads. *Bioinformatics* **34**, 739–747 (2018).

790 **Acknowledgments:** We thank the Columbia University ICM team for the excellent animal care, all members from the Tosches lab for critical input throughout the project, and Darcy Kelley for feedback on the manuscript. We thank Chao Feng and Elena Dvoretzkova (Mayer lab) for the generation of the TrackerSeq libraries and fruitful troubleshooting, Saeed Tavazoie for access to FACS sorting, Lina Habba for help with HCRs, and Susan Brenner-Morton for the FOXP1
795 antibody. Computing resources were provided by Columbia University's Shared Research Computing Facility (NIH grant 1G20RR030893-01 and NYSTAR contract C090171).

Funding: This work was supported by the National Institute of Health (grants R35GM146973 to MAT and 1RM1HG011014 to RS), the Rita Allen Foundation (MAT), the Chan Zuckerberg Initiative (MAT), the McKnight Foundation (MAT), a DFG project grant 549328218 (CM), an
800 EMBO Long-Term Fellowship ALTF 874-2021 (AD), the National Science Foundation (Graduate Research Fellowships to EG and LKVPL), and the Anusandhan National Research Foundation (ANRF/ECRG/2024/006839/LS to SC).

Author contributions: AD and MAT designed the study. AD, EG, and JW collected scRNA-seq data. AD, SC, CL, EG, MAT analyzed scRNA-seq data with input from RS and CM. AD
805 and JW performed histology and imaging. AD and AOG performed birthdating analysis. AD performed injections and electroporations. AD and LKVPL optimized and implemented FACS. PA produced and analyzed axonal tracing data. AD and MAT wrote the manuscript, with edits from CL and SC and feedback from all other authors. CM and RS provided critical feedback on the project. MAT supervised the whole study.

810 **Competing interests:** In the past 3 years, RS has received compensation from Bristol Myers Squibb, ImmunAI, Resolve Biosciences, Nanostring, 10x Genomics, Parse Biosciences and Neptune Bio. RS is a co-founder and equity holder of Neptune Bio.

Data and materials availability: The scRNA-seq data produced for and used in this study will be deposited in the Gene Expression Omnibus (GEO) after journal acceptance. Code
815 used for the analysis of TrackerSeq data is available on <https://github.com/mayer-lab/TrackerSeq>.

Materials and Methods

Animals/sampling

820 *Pleurodeles waltl* embryos, larva and adults were obtained from breeding colonies established at Columbia University. The animals were maintained in an aquatics facility at 20-25 °C under a 12L:12D cycle (93). All experiments were conducted in accordance with the NIH guidelines and with the approval of the Columbia University Institutional Animal Care and Use Committee (IACUC protocols AC-AABF2564 and AC-AABL1550). Embryos and larvae were staged
825 according to (94).

EdU administration

Larvae were deeply anesthetized in 0.02% MS-222 and placed on their back in a petri dish or Sylgard mold. A single EdU injection (2.5 or 5 mg/mL stock solution in sterile 0.9 % saline with FastGreen at a 1:30 ratio) was administered intraperitoneally (50 mg/kg of total body weight),
830 using a glass capillary needle and pressure injection at developmental stage 37, 41, 46, 50, 53 or 55a.

DNA constructs

Some expression vectors used in electroporation experiments were purchased from Addgene: pCAG-mCherry (gift from Jordan Green, Addgene plasmid # 108685) and pCAG-mGFP (gift
835 from Connie Cepko, Addgene plasmid # 14757).

TrackerSeq library preparation and validation

The TrackerSeq plasmid library was produced following the library production protocol from (46). In brief, a 16-base oligonucleotide randomer was cloned into a linearized pCAG-EGFP vector using 12 reactions of HiFi assembly. Subsequently, the reconstituted plasmids were desalted
840 and concentrated. Then, 8 reactions of 4.5 uL barcoded plasmid were mixed with 50 uL NEB-beta 10 electrocompetent cells and electroporated in a 5 mm cuvette at 1.95 kV, 200 W, 25 uF with 3.8-4.0 ms. Transformed bacteria were recovered for 15 minutes and then plated onto 15 cm LB + Amp + Sucrose plates for recovery of individual colonies, then scraped and cultured in 5L LB + Amp + Sucrose media for 3 hours (until OD = 4.8), followed by maxiprep and
845 concentration.

Electroporation

Glass capillary needles were pulled and then broken open using fine forceps (needle tip diameter ranging 5-15 um), backfilled with mineral oil, and then connected to a Nanoject III injection system (Drummond), and filled with plasmid solution. Right before injection, larvae
850 were deeply anesthetized in 0.02% MS-222 and stabilized in a Sylgard mold. The needle was inserted through the skin, in the right lateral telencephalic ventricle, and plasmid solution was pressure injected. At stages 39 or 53, 120 nL or 250 nL plasmid solution was pressure injected at 10 nL/s or 15 nL/s, respectively. For pCAG-mGFP electroporation, a plasmid DNA solution of 1.5 ug/uL was prepared. For TrackerSeq experiments, a DNA plasmid solution of TrackerSeq
855 library (final concentration of 0.8 ug/uL) and pEF1a-pBase (PiggyBac-transposase; a gift from R. Platt) (final concentration of 0.7 ug/uL) was prepared. Fastgreen was added to the plasmid preps at a 1:10 ratio for visualization of the injection site.

Immediately after injection, larvae were placed sideways in a freshly prepared 2% agarose carved mold, filled with ice cold PBS, with two additional carved molds for the electrodes at a
860 distance of 7 mm to one another. The electrode molds were positioned either parallel, or in a 40 degree angle relative to the mold for the larva. Electroporations were performed towards the dorsal walls of the ventricle, with a BTX electroporator (ECM830), using round 5 mm diameter

platinum plate electrodes attached to tweezers (Nepagene, CUY650P5), similar to what was described in (44). 5 50 ms unidirectional pulses with a 1 s interval were applied at 38 V or 46 V
865 at stages 39 or 53, respectively, after which the larvae were allowed to recover.

For TrackerSeq experiments, larvae were screened 48-120 hours after electroporation, and those with a bright GFP positive telencephalon were grown to complete larval development and metamorphosis (3.5 - 6.5 months after electroporation).

Neurobiotin retrograde tracing

870 Iontophoretic injections were conducted by first anesthetizing salamanders in 0.1% MS222, followed by transcardiac perfusion with oxygenated Amphibian Ringer's solution (96 mM NaCl; 20 mM NaHCO₃; 2 mM KCl; 10 mM HEPES; 11 mM glucose; 2 mM CaCl₂; 0.5 mM MgCl₂), as previously described (29). The bidirectional tracer Neurobiotin (VectorLabs SP-1120) was diluted to 5% w/v in oxygenated Amphibian Ringer's solution immediately before each injection
875 and mixed with FastGreen dye (5% w/v, Sigma-Aldrich F7252) to confirm successful tracer injection. This tracer solution was manually loaded into a microneedle (diameter ~10 μm) pulled from capillary glass (1.5mm, Sutter P87). The needle was then mounted to a microelectrode holder (WPI MEH35W15) with a silver wire making contact with the tracer solution. The positive terminal was connected to the needle, which was mounted on a manual micromanipulator for
880 injection (Narishige MM3), and the negative terminal was placed under the head of the salamander at the level of the diencephalon, contralateral to the injection site (in order to draw the tracer into the tissue area of interest). Using anatomical landmarks, the needle tip was inserted into the thalamus, and a positive current was applied with parameters 3 μA, alternating 7 sec on, 7 sec off, for 20 min (according to (95)) using a Midgard Precision Current Source (Stoelting, 51595). Once the injection was completed, the salamander heads were transferred to
885 ice-cold oxygenated Amphibian Ringer's solution to incubate for 24-30 hours. The brains were then extracted and fixed overnight in 4% PFA at 4°C and processed as described below. Labeling was scored manually and localization of Neurobiotin signal was determined using molecular and anatomical landmarks.

890

Tissue processing for (whole mount) IHC and HCR

Animals were first deeply anesthetized by immersion in 0.02% MS222 for larvae, or 0.1% MS222 for post-metamorphic juveniles or adults. From developmental stage 50 onwards, animals were transcardially perfused with ice-cold DEPC phosphate-buffered saline (DEPC-
895 PBS) to remove blood from the brain. Only post-metamorphic animals were additionally perfused with ice-cold 4% paraformaldehyde (PFA) in DEPC-PBS. Brains were dissected, and fixed overnight in 4% PFA in DEPC-PBS at 4 °C. Brains were then dehydrated (40%, 60%, 80%, 100%, 100% methanol in PBS-DEPC, 15 min each at room temperature (RT)) and incubated in 100% DCM overnight at RT, washed twice in 100% methanol and stored at -20°C until further
900 processing.

HCRs with and without EdU detection were performed as described in (45). Specifically, brains were stained as whole-mount preparations, embedded in 4% agarose in Tris-HCl (500 mM, pH7.0) and sectioned at 70 μ m using a vibratome. Sections were then incubated in DAPI in Tris-HCl for 30 min, and mounted in Fluoromount-G® Mounting Medium (SouthernBiotech) or DAKO fluorescent mounting medium (Agilent Technologies). HCR-3.0-style probe pairs against *Dmrt3*, *Eomes*, *Frmd8*, *Gad2*, *Meis2*, *Nfia*, *Nts*, *Sfrp1*, *Slit2*, *Sp8*, *Wnt8b*, *Zbtb20* were designed using `insitu_probe_generator` (96) and ordered from IDT, and 6 pmol was added to the probe hybridization buffer (Molecular Instruments) for incubation. For co-staining with antibodies SATB1 (1:50, abcam ab51502), PH3 (1:500, Sigma 06-570) or GFP (1:500, abcam ab13970), the primary antibody was added to the amplification buffer with hairpins, and the secondary antibody being either goat anti-mouse IgG Alexa 488 antibody, donkey anti-chicken IgY Alexa 488 (1:500, Jackson ImmunoResearch), or goat anti-rabbit IgG Alexa 546 (1:500, Invitrogen) to the overnight wash in 500 mM Tris-HCl, similar to what has been described for the GFP antibody in (45). For the detection of Neurobiotin, Streptavidin conjugated to Alexa Fluor 647 (1:1000, Invitrogen S32354) was added to the amplification buffer.

Immunostainings were performed on 70 μ m vibratome sections. Briefly, sections were permeabilized in PBS supplemented with 0.2% Triton X-100 (PBST) for 30 min at RT, then blocked in blocking buffer (2.5% BSA, 2.5% sheep serum, 50 mM glycine in PBST) for 30 min at RT and incubated with primary antibody solution (10 mM glycine, 0.1% H₂O₂ in PBST) for 1-3 nights at 4 °C. Tissue sections were then washed 3 x 15 min in PBST at RT, incubated with secondary antibody solution (DAPI 1:1000 in PBST) for 2 hrs at RT, and again washed for 3 x 15 min before mounting in Fluoromount-G® Mounting Medium (SouthernBiotech) or DAKO fluorescent mounting medium (Agilent). Primary antibodies used are rabbit anti-FOXP1 (1:40000, custom antibody generated by Susan Brenner Morton (97)), mouse anti-NFIA (1:10, DSHB PCRP-NFIA-2C6), mouse anti-NEUN (1:500, Sigma-Aldrich MAB377), rabbit anti-SOX2 (1:500, abcam ab97959), and secondary antibodies goat anti-rabbit IgG Alexa 546 or goat anti-mouse IgG Alexa 647 (1:500, Invitrogen). The NFIA antibody required antigen retrieval, which was performed after permeabilization by incubation in a 10 mM sodium citrate pH6 buffer in a 70 °C water bath for 30 min, followed by 2 5 min washes in PBST at RT.

930 Confocal microscopy and EdU quantification

All images were acquired using a Zeiss LSM800 confocal microscope, and processed in Fiji. HCR images presented in grey were generated by setting the channel colors to Grays and inverting the LUTs of the HCR and DAPI channels separately, and then overlaying both channels in Adobe Photoshop and adjusting the transparency of the DAPI channel.

935 For quantification of the molecular identity of EdU cells, sections across the anterior-posterior axis of the anterior dorsal pallium (until the ventricle of the two telencephalic hemispheres merges in the coronal section, 8-14 hemispheres per animal) were imaged as tiled z-stacks (6 images at 4 μ m interval). Using the Cell Counter Plugin in Fiji, all EdU cells in the dorsal pallium

were manually counted and scored for expression of *Nts* and *Frmd8*. Cells were considered
940 positive for EdU when the intensity of the label was above background levels, regardless of the
pattern within the nucleus. Cell proportions were then calculated, and data presented as mean \pm
SD (n = 4 animals analyzed for each stage, except for stage 55a for which n=5).

Head or brain dissociation and single-cell capture

To increase the comprehensiveness of our previously published single-cell RNA-sequencing
945 developmental dataset (29), we dissociated 40 heads from stage 30, and 25 heads from stage
33 embryos. In addition, we dissociated the telencephalic vesicles of an additional 6 stage 50,
and of 6 stage 53 larvae, and the telencephalon and diencephalon of 15 stage 55a larvae. The
latter received an intracerebroventricular AAV-PHP.eB virus injection for driving the expression
of eGFP under the CAG promoter at either stage 37, stage 41 or stage 51 as described in (45).
950 Dissociation was performed according to (29), with a small modification for the stage 30 and 33
heads, which were only incubated for 15 min in the enzymatic dissociation cocktail. All
dissociated cells were multiplexed using 4 distinct Cell Multiplexing Oligos (10x Genomics 3'
CellPlex Multiplexing kit) per stage, prior to GEM formation.

Sample collection for TrackerSeq libraries

We separately collected the telencephalon, and the diencephalon and midbrain of
955 electroporated brains from salamander juveniles (right after metamorphosis) and pooled tissue
chunks from two animals before performing papain dissociation according to (29) with minor
modifications to recover as many cells as possible. All filters were pre-wetted and post-washed
with 1-5 mL fresh carbogenated calcium-free Hibernate A media (BrainBits), centrifugation was
960 performed at 500 x g, and after the density gradient centrifugation step, the cell pellet was
resuspended in calcium and magnesium free PBS supplemented with 1% BSA and transferred
to FACS tubes. All tubes for filtering the cells, and the FACS tubes were coated overnight with
2% BSA in calcium and magnesium free PBS at 4 °C. To enrich electroporated cells, we
performed fluorescence activated cell sorting using a Bio-Rad S3e Cell Sorter (ProSort software
965 version 1.6.) with a 100 um nozzle. Non-eGFP-expressing brain tissue from control siblings was
used as a negative control for excluding background fluorescence and to set the gate on forward
scatter. The positive diencephalon and midbrain samples were used to set the lasers and gates
of the eGFP population. Sorted cells (between 2300 and 13000 cells per sample) were collected
in bulk in coated low-profile PCR 8-strips with temperature control set to 4 °C. Cells were
970 processed on the 10x Genomics Chromium platform.

Analysis single-cell RNA sequencing data

Read alignment

For all newly acquired samples, reads were aligned to the combined *Pleurodeles waltl*
transcriptome (29) using Alevin (Salmon v1.6.0) (98). The transcriptome was supplemented with
975 itr-eGFP sequences for aligning the stage 55a libraries. Library type was set to automatic, and

keepCBFraction was set to 1, whereas all other parameters were set as default. Developmental libraries were multiplexed using the 10x Genomics 3' CellPlex Multiplexing kit, and multiplex tag reads were assigned using Alevin as well.

Data QC and filtering

980 Count matrices obtained after alignment with Alevin were imported in the R package Seurat
(version 4.3.0.1 (99)) to generate individual Seurat objects. The objects were first demultiplexed
independently based on the identity of the Feature Barcode oligonucleotides introduced using
the 10x Genomics 3' CellPlex Kit, and only singlets were retained. These objects were then
985 filtered to remove droplets with low UMI counts (less than 700 genes per cell for all libraries
except stage 30, which was filtered to remove cells with UMI counts below 2000), and high
mitochondrial content (more than 15% mitochondrial genes per cell). Datasets were then pooled
in steps depending on when the samples were generated and further filtered using Seurat 4.1.0.
Specifically, after Louvain clustering, low-quality cells were removed using a Support Vector
Machine (SVM) classifier (R package e1071) as described in (13). Low-quality clusters (number
990 of genes per cell below average of the dataset, percentage of mitochondrial genes above
average of dataset, and absence of cluster-specific marker genes) were first identified, and 10%
of cells from these clusters, together with 10% of cells from the rest of the dataset were used to
train the classifier. The trained SVM classifier then identified low-quality cells across each
dataset, which we removed. All SVM-cleaned, pooled datasets were finally merged, also
995 including our already published dataset (29) to obtain a final Seurat object of 127,488 cells.

Clustering

The full 127,488-cell dataset was initially clustered and analyzed using the R package Seurat
4.1.0 (99). CellCycleScoring was applied, after which the raw counts were normalized using
SCTransform (100, 101), while regressing the data for the number of UMIs per cell,
1000 developmental stage, percent mitochondrial genes, G2M and S scores. The top 3000 variable
genes were used and a principal component analysis (PCA) was performed, after which the first
180 principal components were used for clustering and UMAP embedding. The default
clustering method was used, with a resolution of 1.5. Clusters were then annotated based on the
expression of marker genes, and label transfer (see below). This dataset was analyzed in more
1005 detail and at higher resolution for specific clusters. To study the competence of dorsal progenitor
cells, pallial progenitors were subsetted in steps based on marker gene expression (presence of
Slc1a3, *Foxg1*, *Emx1*, absence of *Dlx1/2*, *Gsx2*, *Nkx2.1*, *Ascl1*, *Otx2*, *Cdh6*). Clusters with
highly expressing *Slc1a3*, *Gfap*, *Sox2* and *Sox9* cells were then used for spatial and temporal
analysis of radial glia progenitors (see below), while clusters with highly expressing *Eomes* cells
1010 were analyzed for the presence of intermediate progenitors. For the latter, raw counts were
normalized using SCTransform, regressing for the number of UMIs per cell, percent
mitochondrial genes and developmental stage (not cell cycle score). 45 principal components
were used for clustering and UMAP embedding at a resolution of 0.5. To study neuronal
differentiation of the pallium, we implemented a two-step process. First, telencephalic

1015 progenitors were selected from the progenitor object, and telencephalic neurons from the full
dataset based on a combination of marker genes (*Foxg1*, *Neurod2*, *Neurod6*, *Dlx5*, *Dlx6*,
Snap25) and labeltransfer (see below). Raw counts from the telencephalic cells were
normalized using SCTransform, regressing for number of UMIs per cell, developmental stage,
percent mitochondrial genes, G2M and S scores, 150 principal components were used for
1020 clustering and UMAP embedding at a resolution of 1.5. From the telencephalic dataset, a
dataset including only pallial cells was extracted using a combination of marker genes and
labeltransfer. Raw counts were again normalized using SCTransform, regressing for number of
UMIs per cell, developmental stage, percent mitochondrial genes, G2M and S scores, 125
principal components were used for clustering and UMAP embedding at a resolution of 1.5.

1025 **Label transfer**

To annotate the developmental clusters, Seurat's Label transfer was performed using the adult
Pleurodeles dataset (29, 42). Cluster TEGLU7 in medial pallium was split in two after subsetting
and running FindAllMarkers, since part of this cluster (TEGLU7.2) expresses *Nts* at high levels
with cells located in the superficial MP, while neurons in cluster TELGLU7.1 do not express *Nts*
1030 (**fig. S1C,D**). The Label Transfer algorithm identifies transfer anchors between two data sets,
allowing comparison of cell type identities between the two. To increase the matching of cell
types, Label transfer was performed iteratively. Hereto, the full adult dataset (29) was used as
first reference, and the stage 55a dataset as first query. Subsequently, the annotated stage 55a
dataset was used as a reference for identifying cell identity in the stage 53 object, and so on.
1035 For all transfers, the function FindTransferAnchors was run using `dims = 20`, and `k.anchor = 5`,
and the function TransferData was run using `k.weight = 20`.

Heterogeneity of pallial progenitor cells

We first subsetted the pallial dataset to clusters with high *Slc1a3* expression (**fig. S8A,B**). Within
this subset, we identified a cluster of cells with a strong astroglial signature (high expression of
1040 *Acan*, *Aqp4*, and low expression of *Mcm2* and *Mcm5* (**fig. S8A-C**)). This cluster represents
radial glia cells that are differentiating into ependymoglia, and therefore was removed for the
rest of the analysis. To characterize the heterogeneity of pallial progenitor cells, we calculated
the variance of the normalized data. The data was processed using SCTransform `vst.flavor="v2"`
(100). We calculated the first 50 principal components using the RunPCA() function in Seurat
1045 (99) and then retained the 14 first principal components which captured at least 1% variation
each. To identify which factors are associated with each principal component, we calculated
pearson correlation between the principal components and various technical and biological
factors associated with each cell including cell cycle score "G2M.Score", "S.Score", total RNA
content ("nCount_RNA"), number of genes expressed in each cell ("nFeature_RNA"),
1050 percentage of mitochondrial and ribosomal genes expression ("percent.mt", "percent.ribo") of
the cell, and developmental stage of the sample ("Stage") (**fig. S8D**).

To adjust for differences arising from technical and biological factors we re-ran SCTransform with `vst.flavor="v2"` and regressed these factors by using `vars.to.regress = c("G2M.Score", "S.Score", "nCount_RNA", "nFeature_RNA", "percent.mt", "percent.ribo", "Stage")` and also re-ran PCA. Next, we fit a principal curve which represents an ordered 'spatial trajectory' for each cell based on their expression profile using the `principal_curve` function in the `princurve` R Package (102, 103) using options `smoother = 'lowess', f = 1/3` and `stretch=2`). We defined a 'mediolateral score' as the length of the arc from the beginning of the curve to the point where the cell projects onto the curve. Since there is no directionality associated with the curve, we defined an explicit starting point based on the expression of *Wnt8b*, such that its expression is negatively correlated with the 'mediolateral score'. *Wnt8b* is a canonical marker for medial pallium, confirmed in the developing *Axolotl* brain using spatial transcriptomics (51, 52) and as such, its expression should be high in the medial cells. To identify genes that vary across the mediolateral axis, we used the `fitGAM` function in the `tradeSeq` package (104) using `nknots = 3`. To limit the analysis to highly informative genes, we ran `fitGAM` with mediolateral scores as the pseudotime with only genes that had a residual variance of at least 0.5 after running SCTransform. To assign explicit spatial labels to the progenitors, we performed a hierarchical clustering using the genes that are differentially expressed across the mediolateral trajectory. We used the `hclust()` function with `method="ward.D2"` to perform hierarchical clustering in R; the tree was cut at `h=350` to obtain 10 clusters and isolate the dorsal pallium progenitors.

Temporal patterning of dorsal pallium progenitor cells

To characterize the genes involved in temporal patterning of dorsal pallium in salamanders, we used a scoring strategy similar to our medio-lateral score. Following our spatial analysis and hierarchical clustering, we subsetted out the dorsal pallium progenitors (fig. S8E). To reprocess the subsetted DP population with SCTransform, we regressed out non-temporal factors that contribute to heterogeneity using `vars.to.regress = c("G2M.Score", "S.Score", "nCount_RNA", "nFeature_RNA", "percent.mt", "percent.ribo")`. We fit a principal curve as previously described (fig. S9A). We defined a 'temporal score' as the length of the arc from the beginning of the curve to the point where the cell projects onto the curve. For processing the mouse neocortical progenitors, we used SCTransform with `vars.to.regress = c("G2M.Score", "S.Score", "nCount_RNA", "nFeature_RNA", "percent.mt", "percent.ribo")`. To identify genes expressed differentially across the temporal trajectory, we used the `fitGAM` function with temporal scores as the pseudotime. Temporally variable genes were identified with a log fold change of 2 and adjusted p-value < 0.05. To identify conserved temporal genes across salamander and mouse, we subsetted the list of temporally variable genes to only include one-to-one orthologs that are expressed in both the species and have a residual variance of at least 0.5. Gene ontology analysis was performed for upregulated and downregulated genes separately using the `clusterProfiler` package (105) with the universe genes as the list of one-to-one orthologs that had a residual variance of at least 0.5 in both mouse and salamanders.

1090 **Analysis of developmental trajectories**

To reconstruct transcriptional trajectories that underlie specification and differentiation of pallial neurons, we used the R package URD (v1.1.1) (60). The pallial object generated previously contains some excitatory neuronal cell types present in the telencephalon, that originate from extra-pallial territories (e.g. *Sim1+ / Otp+* neurons in the amygdala, excitatory neurons in the septum, and some mitral and tufted cells in the olfactory bulb). Since their complete trajectory cannot be reconstructed, we removed these neurons for the URD dataset. To increase the number of mature cells, we added differentiated pallial neurons from our adult object. In total, we analyzed 2996 radial glia cells, 13483 immature neurons, and 13840 mature neurons spanning the AMY, VP, DP, LP, MT, and MP clusters.

1095 First, we calculated a diffusion map using the `calcDM` function in URD with `knn=200` and using `sigma.use=NULL` which automatically determines the most optimal sigma. We assigned a subset of cells with high expression of *Slc1a3* as the root cells after removing the gliogenic cells expressing high *Aqp4*. We then used the root cells and simulated diffusion from root cells to all other cells to calculate the pseudotime. To simulate diffusion, we used the `floodPseudotime` function in URD with `n=50` simulations and using `minimum.cells.flooded=2` so that the simulation stopped if 1 or no cells were newly visited in a given iteration. The tips were defined to be the cells that were previously annotated to be mature cells (assigned a `TEGLU*` label) using our label transfer approach. We then used the `pseudotimeWeightTransitionMatrix` function with `optimal.cells.forward = 40`, `max.cells.back = 80`, `pseudotime.direction = "<"` to identify the slope and inflection point of the logistic function which is used to bias the transition probabilities using `pseudotimeWeightTransitionMatrix` function. To simulate random walks on the cell-cell graph from the root cells to the tip, we used the `simulateRandomWalk` function performing 10,000 random walks per tip (`n.per.tip = 10000`). To generate the dendrogram layout, we used the `buildTree` function with `divergence.method = "preference"`, `cells.per.pseudotime.bin = 25` and `bins.per.pseudotime.window = 8`. To create the forced directed layout, we used the `treeForceDirectedLayout` function with `num.nn = 100`, `cut.unconnected.segments = 2`.

1100 Genes differentially expressed between URD segments were computed using the `FindAllMarkers` function in Seurat, and filtered to retain genes with adjusted p-value < 0.001 that were expressed in at least 20% of at least one segment, and with $\text{abs}(\text{pct}\$1 - \text{pct}\$2) > 0.15$. From this list, we then identified genes with specific expression in SL or DL trajectories by computing genes expressed in segment 6 (SL) but not in segments 45, 44, 5, 9, and 37 (DL), and vice versa (see fig. S10A for segment labels). The heatmap in Fig. 5D shows all genes with differential expression along pseudotime except these SL and DL-specific trajectory genes, whereas Fig. 6B shows only the SL and DL-specific trajectory genes.

1115 To generate the heatmaps in Fig. 5D and 6B, gene expression was smoothed by computing moving averages along pseudotime, followed by spline fitting (function `geneSmoothFit` in the URD package). Genes were then ordered according to the relative peak of expression along

pseudotime, following the approach described in Raj et al. (106). For each gene, smoothed expression data were scaled to the max expression for that gene before plotting.

1130 To identify genes with differential expression at URD branchpoints, we used the FindMarkers
function in Seurat. For mouse, we used the neocortex developmental data and URD analysis
from Di Bella et al. (53), comparing segments 15 (IT branch) and 17 (non-IT branch). For
salamander, we took segment 45 (the segment in common between the three anterior DL cell
types) and cells in segment 6 (SL cells) with the corresponding pseudotime values. We filtered
1135 these lists of differentially expressed genes to retain only transcription factors (mouse and
salamander one-to-one orthologs) with $\text{avg_logFC} > 1$ (mouse) or $\text{avg_logFC} > 1.2$ (salamander),
and expressed in at least 25% of cells in one of the two segments.

To analyze the expression of gene modules in salamander developmental trajectories, we used
the gene modules computed by Gao et al. (69) from a developmental cell type atlas of the
1140 mouse visual cortex. For each gene module, salamander-mouse one-to-one orthologs were
identified using eggnoG mapping. After this step, only modules with at least 5 genes were
retained. Expression enrichment for each module was computed using the AUCell_run function
in the AUCell package (107).

Gene specificity index correlations of salamander and mouse cells

1145 Correlations between developing salamander and mouse cells were computed following an
approach described in (13). Briefly, average gene expression from log-normalized data from the
developing mouse neocortex (data from (53)) and the developing salamander dorsal pallium
were computed using the AverageExpression function in Seurat. Next, for each species, we
computed differentially expressed genes (FindAllMarkers function in Seurat,
1150 $\text{logfc.threshold}=1.5$). From these lists of differentially expressed genes, we identified the
salamander-mouse one-to-one orthologs, and then took the union of the two lists (5743 genes).
Gene specificity matrices for salamander and mouse data were computed as described in (13),
and then pairwise Spearman rank correlations between cell classes were computed from these
matrices. Statistical significance was assessed with a permutation test, after shuffling gene
1155 expression values 1000 times across cell classes.

Classification of mouse neocortical cells using salamander SL and DL marker genes

To assess how gene signatures derived from SL (TEGLU20) and DL neurons (TEGLU8,
TEGLU10, TEGLU11) in salamander DP discriminate cellular identities in the mouse cortex, we
first identified differentially expressed genes between salamander SL and DL neurons using the
1160 FindAllMarkers function from the Seurat R package (parameters: $\text{test.use} = \text{"roc"}$), and then
filtered the list to keep only genes expressed in at least 30% of cells of at least one of the two
groups, with $\text{abs}(\text{avg.logFC}) > 1.1$ and with a ROC score below 0.4 or above 0.6. This resulted
in 258 marker genes, of which 148 expressed in SL and 110 in DL. Next, we identified mouse
one-to-one orthologs of these genes using eggnoG-based mapping. This resulted in 131 SL
1165 genes and 88 DL genes. We then used these to compute gene module enrichment in mouse

cells. From the Allen Brain Cell atlas (71), we selected all telencephalic glutamatergic subclasses (defined by the expression of *Foxg1* and *Slc17a6* or *Slc17a7*) and downsampled the dataset to 200 cells per cell subclass. Next, we used AUCell (107) to compute expression enrichment of SL and DL markers for each subclass in the mouse (fig. S12).

1170 Next, we filtered the mouse Allen Brain Cell atlas dataset to keep only neocortical glutamatergic
cell "subclasses" (according to the Allen Brain Cell atlas taxonomy) and the expression values of
the mouse one-to-one orthologs of salamander SL and DL marker genes (computed as
described above). Count data were log-normalized and then scaled. Next, we trained
1175 multinomial logistic regression models with L2 regularization ($\alpha = 0$) using the glmnet
package's `cv.glmnet` function (family = "multinomial", 20-fold cross-validation). Models were
trained to predict one of three classification schemes in mouse metadata: "layer", "birthdate",
and "projection". These labels were assigned according to the metadata of the Allen Brain Cell
atlas (for birthdate, L5 and L6 neurons were "early born", and the rest "late born"; for projection,
we used IT, ET, CT, and NP labels in the original dataset). We evaluated model performance
1180 using a bootstrap approach with 100 iterations. In each iteration, a subset of cells from the
mouse were resampled with replacement using `sample()`, and the remaining out-of-bag (OOB)
cells were used for testing. Normalized Mutual Information (NMI; computed via `NMI` from
`aricode`) was calculated for each replicate. To assess whether classification performance
differed significantly for the three sets of labels, we used the Kruskal–Wallis rank sum test, a
1185 non-parametric alternative to one-way ANOVA that does not assume normality, followed by
pairwise post hoc comparisons using Dunn's test (`FSA::dunnTest()`) with Benjamini–Hochberg
correction for multiple testing.

TrackerSeq analysis

1190 **Estimation of TrackerSeq library diversity**

From the concentrated TrackerSeq plasmid library, PCR amplification of the variable barcode
sequences was performed using a P7-containing Read2 and a P5-containing custom reverse
primer, at a low cycle count (~18) and purified using 2-sided selection for the ~330 bp length
product with SPRI magnetic beads. Over 6.7M NGS reads were performed on the library, with
1195 almost 5.4M unique barcodes detected. The barcodes were read-extracted and clustered using
`Bartender v1.1 bartender_extractor_com` and `bartender_single_com` (108) to remove putative
barcode reads that were likely the result of PCR amplification or NGS sequencing errors using a
hamming distance of 2. This resulted in at least 2.6M unique barcode sequences, indicating that
the TrackerSeq library used has minimum diversity well into the millions.

1200 **Preprocessing of TrackerSeq Barcodes**

Dedicated TrackerSeq barcode libraries were generated from an aliquot of the 10x Genomics
cDNA by amplification with indexed P5 and P7 primers as in (46). The resulting NGS fastq files

were paired, quality-filtered, and assigned to unique cell barcodes using the UMI-tools 'extract' and 'whitelist' funmmum hamming distances. Complete barcodes with valid UMIs and cellbcs, and including the fixed sequence handle and spacers were clustered using umi-enabled Bartender v1.1 bartender_single_com (108) to remove putative barcode reads that were likely the result of PCR amplification or NGS sequencing errors. This was done using a hamming distance of 5, since the fixed handle sequence increases minimum hamming distances. Resulting raw barcode sequences and their cluster centroids (the consensus sequence from clustering) were mapped as a dictionary for cluster scores with a quality score of <0.8 (indicating that for each UMI of an erroneous barcode, ~3x the number of centroid UMIs are observed). Unmapped barcodes were retained in the dataset as unique signatures, which would cause only splitting of clones, and not result in bundling errors, or false positives. Unique combinations of lineage barcodes, cellbcs, and UMIs were aggregated, and UMIs above this threshold counted for each unique pair of lineage barcode and cellbc. The barcode data was filtered for minimum number of reads = 5 and minimum number of UMIs = 3.

To determine clonal membership of cells, we have employed a network-based analysis which treats cells as nodes containing barcodes, with edges connecting each cell that share at least a single barcode. Each cell-cell edge receives a weight according to the following equation:

$$(Intersection(LBCs_{cell1}, LBCs_{cell2}) / (LBCs_{cell1} + LBCs_{cell2})) * 2$$

The metric scores the shared profile of barcodes present in both cells similar to a Jaccard distance, but with increased penalty for cell pairs where one member of the pair has few barcodes and the other has many barcodes. For each collected dataset, these scores are graphed as a histogram (e.g., counts of cell-cell edges with a given weight) (**fig. S3**).

After edge weighting, all connected components (i.e., cells that are connected by edges) within the network are determined for stepwise weight thresholds from 0 to 1, where the edges with weights below the threshold are removed from the network, filtering membership of connected cell nodes. With this method, cells connected by the strongest lineage barcode signatures are preserved, while those with partial signatures such as those caused by PCR amplification errors or repeat sampling of barcodes are omitted. Since the noise level of each experimental dataset depends on the accumulation of technical noise over multiple experimental steps (**fig. S3**), it is necessary to select a cutoff threshold for each dataset.

Heuristic indicators such as clone number and size statistics were used to mitigate the effect of noise present in unfiltered barcode signatures to optimize recovery of true positives while excluding false positives. Over-filtering the networks would lead to a loss of multi-cell clones that provide meaningful biological signals, as shown by the counts of multicell clones present in the data. Therefore, for each dataset in the TrackerSeq experiment, we selected the minimum threshold value where the clone size distribution was stable. The selected thresholds are shown in each of supplementary **figures S3, S4 and S5**. Connected networks from each dataset were assigned as clones. In addition, as a strict control experiment, we filtered the networks for only

perfect lineage signatures (i.e., similarity score = 1) to ensure that commonly observed lineage relationships are retained in the data. We confirmed that this strictly filtered dataset supports the claims made in this paper despite a fractional loss of lineage clones.

Analysis of clonal information in transcriptomic data

1245 Clone assignments from the selected threshold levels were mapped into the Seurat transcriptome data. 1988 cells out of 2556 detected in the lineage matrix were successfully mapped. We counted the number of clonal intersections and the number of cells from those intersections (**Supplementary Tables 1 and 2**).

To evaluate the significance of cell lineages shared across annotated groups, we calculated a
1250 coupling z-score for each pairwise comparison of cell categories according to previous work (46, 47) with 5000 permutations of data shuffling on the pooled lineage data from 8 replicates. Z-scores shown in Figure 2F describe the number of standard deviations between the observed clonal counts and the aggregate mean of shuffled permutations. Positive scores indicate observation of more shared clones than chance, indicating positive lineage coupling, while
1255 negative scores indicate fewer observations than chance, indicating negative lineage coupling. Z-scores > 2.58 have equivalent p-values ≤ 0.01 and > 3.29 with $p \leq 0.001$.

Correlations using `np.corrcoef` on the between-group scores were performed along with hierarchical clustering using 'average' from `scipy.cluster` (**fig. S6A**).

Some lineage tracing experimental replicates had substantially higher clone counts and
1260 coverage of cell types within traced cells (**fig. S2C**). We performed z-scoring using the same method on data for each replicate, then converted these z-scores into percentiles so that inter-sample differences were normalized. For cell-cell pairs that had coverage across all experimental replicates, we used `pingouin.rm_anova` to perform repeated-measures ANOVA testing between the pairwise lineage counts data for dataset vs. cell-pair assignment. The
1265 significant result, $f = 3.21$ equating to $p = 0.015$, demonstrated that the variance between cell-cell pair groups was significantly greater than the variance across replicates for each pairwise comparison (**Fig. 2H**).